Final Report: Marshall Plan Scholarship

Electronic Correlations in Kagome Lattice

Research Exchange with University of California, Davis

January 30, 2018 - July 1, 2018

Supervisor at Home University
Prof. Dipl. Dr. Karsten Held
Institute of Solid State Physics
Technical University of Vienna
Wiedner Hauptstr. 8
1040 Wien
Telephone: +43 (1) 58801 - 137 10
Email: karsten.held@tuwien.ac.at

Supervisor at Host University
Prof. Dr. Richard T. Scalettar
Department of Physics
University of California Davis
1 Shields Ave
Davis, CA 95616
Telephone: +1 (530) 400 – 3563
Email: scalettar@physics.ucdavis.edu

by

Klaus Steiner, BSc

Vienna, Friday 28th September, 2018

Abstract

The aim of this project is the investigation of electronic correlations in the intermediate region between the metallic and insulating phase of the frustrated Kagome lattice. Most previous studies address the ground state of the Heisenberg model on the Kagome lattice, and therefore only the purely insulating phase. However, we go a step further by studying the Hubbard model on the Kagome lattice and thus including metallic contributions. We solve the Hubbard model with the determinant quantum Monte Carlo (DQMC) method and compare to results of the dynamical mean field theory (DMFT). First we study the half-filled system across the range of the Mott-Hubbard metal-insulator transition, and then the electron-doped system, where the chemical potential is in the center of the flat band. In various post-processing steps we calculate the k-integrated spectral functions, the k-resolved spectral functions, the equal-time magnetic structure factors and the dynamic magnetic structure factors.

Contents

Chapter 1

Introduction

Geometrical frustration of lattices gives rise to interesting phenomena, such as e.g. spin liquids. One famous lattice of this type is the Kagome lattice which is one of the simplest frustrated lattices with the coordination number of 4. One common model which is used to describe spin liquids is the Heisenberg model. Numerous studies have addressed the ground state of the Heisenberg model on the Kagome lattice. One important question, most of them are trying to answer is, if the spin excitation spectrum is gapped, which in turn defines the nature of the spin liquid ground state. A gapped spin liquid ground state in Kagome would give rise to Z_2 topological states, which are in the focus of current research. Such topological states could have applications in quantum computing, due to the long-range entanglement and they could also be used as high-temperature superconductors because of their stability stemming from the topological protection. Finding the solution of these problems is hard, because an analytical solution is not possible, and numerical solutions are challenging as well. In order to solve the Heisenberg model on the Kagome lattice, various methods can be applied and because of the different approximations used, the results are also different. Indeed, some methods show a gapped ground state, whereas other methods claim a gapless one. Therefore, it is still not clear whether the ground state is gapped or not. This discrepancy remains unresolved also on the experimental site: there are papers vouching for a gapless ground state[30, 43] as well as for gapped ground states[11, 55, 45].

One other interesting feature of Kagome's electronic structure is the flat band.

Flat bands pertain to non-dispersive states and are also appearing in bipartite lattices with unequal number of sites in the sub-lattices[21, 7]. For this type of lattice Lieb's theorem[31] holds which says that a uniform onsite energy is turned on at half filling, the ground state has a non zero spin and therefore, is ferrimagnetic. Such Lieb lattices are not frustrated. Hence, Lieb's theorem does not apply for the Kagome lattice and therefore we will explore the magnetism of flat bands beyond this theorem.

On the experimental site, it is very hard to actually realize a Kagome lattice. Usually, the Kagome lattice appears within a three dimensional structure as a sublattice layer. Most problems of creating a Kagome lattice involve the growing process, where the crystal is easily polluted with defects and impurities. So far, only insulating compounds have been realized, which is why most of the theoretical studies for the Kagome lattice are done with the Heisenberg model and therefore only considering magnetic interactions. Growing such insulating structures is challenging but possible. However, to grow a metallic Kagome lattice is even more complicated and not realized yet. Generally, a way to go from an insulating compound to a metallic one is to substitute some of the atoms. For instance when using cuprates, one can chemically substitute atoms that are in between the CuO_2 layers (e.g. replace La by Sr) and the effect is to dope the CuO_2 layers. In this way, the insulating antiferromagnet can be tuned into a superconductor. However, this is not possible for Kagome: First, chemical replacements are hard to do and second, even if chemical replacements work, one would face the problem, of disorder: impurity atoms will sit right in the Kagome lattice itself instead of going into the interlayer space.

Cuprates can be described with the Hubbard model which allows not only spin-spin interactions, but also the hopping of electrons between lattice sites and therefore, can be used to describe metallic systems. The difficulties of actually realizing a metallic Kagome compound makes it worth studying the Hubbard model on Kagome lattice to see, if new interesting physics would arise and thus, metallic Kagome could have an application. In this project we were especially interested under which circumstances the electronic system undergoes phase transitions within the intermediate coupling regime between the pure metallic phase and the insulat-

ing spin liquid region. In particular, we study the behavior of the Hubbard model for different interaction strengths and different temperatures.

In order to solve the Hubbard model, describing a correlated system, different techniques have been developed. Some very fundamental distinct methods are the determinant quantum Monte Carlo (DQMC)[5] and the dynamical mean field theory (DMFT)[18] with its diagrammatic extension dynamical vertex approximation (DΓA)[17]. We investigate three major parts: the metal-insulator transition at half filling and magnetic properties by looking at the one-particle spectra and spin-spin correlation functions. And finally the spin-spin correlations at the filling corresponding to the half-filled flat band.

Chapter 2

Models and Methods

This chapter introduces the models and methods used in this work. We start with a recapitulation of the basics of quantum field theory and then turn to the Hubbard model and Kagome lattice. After that, we describe the two methods determinant quantum Monte Carlo (DQMC) and dynamical mean-field theory (DMFT). Finally, we explain the analytic continuation method - the Maximum Entropy method, used in post-processing to obtain dynamic correlation functions.

2.1. Quantum Field Theory

This section is a short reminder of the most important tools used to describe quantum many-body systems. The fundamental apparatus describing such systems is based on Green's functions and Feynman diagrams. Green's functions are widely used in physics, in particular in field theories to describe the interaction between particles, and are one of the standard tools in modern physics. In condensed matter physics, the energy scales are usually non-relativistic and therefore we do not have to worry about a covariant formulation and the equations take a simpler form than in general Lorentz-invariant field theories. This introduction follows the text book by Zagoskin[2].

2.1.1. Green's Functions

Let us start with the definition of a Green's function and a propagator. A Green's function $G(x, x'; t, t')$ is a solution of a linear differential equation and obeys

$$\mathcal{L}(x,t)G(x,x';t,t') = -\delta(t-t')\delta(x-x') \tag{2.1}$$

where $\mathcal{L}$ is a differential operator of a linear differential equation. This definition is very abstract, but we can interpret the Green's function in a more physical way. For this we introduce the following definition of a propagator $K(x,t;x',t')$

$$\psi(x,t) = \int K(x,t;x',t')\psi(x',t')\,, \tag{2.2}$$

which propagates a wave ψ from location x' and time t' to location x and time t. If the propagator fulfils the causality principle, the following applies: $K(x,t;x',t') = 0$ for $t < t'$ and $K(x,t;x',t') = \delta(x-x')\delta(t-t')$ for $t = t'$ to yield again the wave function $\psi(x,t)$. To see the connection between Green's function and propagator we take a look at the Schrödinger equation and reformulate it into

$$\underbrace{\left[i\hbar\frac{\partial}{\partial t} - \mathcal{H}(x,t)\right]}_{\mathcal{L}_\psi}\psi(x,t) = 0\,, \tag{2.3}$$

where we defined the linear differential operator $\mathcal{L}_\psi$ of the Schrödinger equation. By plugging in Equation (2.2) and applying the chain rule on it, one can seen, that the propagator must satisfy

$$\mathcal{L}_\psi K(x,t;x',t') = i\hbar\delta(x-x')\delta(t-t')\,. \tag{2.4}$$

Besides the pre-factor, this is the definition of the Green's function in Equation (2.1). Hence, we can interpret the Green's function, which solves the Schrödinger equation, as a propagator for location x and time t to location x' and time t'. The above equations are for single particles at zero temperature. However, we would like to extend these methods to describe many particles at finite temperature. To calculate realistic systems we have to deal with $\sim 10^{23}$ particles, which makes it

impossible to describe all of the particles. But even if we could calculate every particle at every time point, we would not really benefit from it. It is more important to know, how a system reacts under a perturbation and this is essentially what Green's functions telling us. We can interpret them as a perturbation by "removing" a particle at (x,t) and "inserting" it again at (x',t'). Let us introduce the time evolution operator

$$\mathcal{U}(t) = \mathcal{T} e^{-\frac{i}{\hbar}\int_0^t d\tau \mathcal{H}(\tau)}, \tag{2.5}$$

which moves the wave function from time 0 to time t. The Wick time ordering operator $\mathcal{T}$ ensures chronological ordering of the integrals when expanding the exponent. With this operator we can now relate a wave function between any time points t and t' by

$$\psi(t) = \mathcal{U}(t)\mathcal{U}^\dagger(t')\psi(t') = \mathcal{S}(t,t')\psi(t')\,, \tag{2.6}$$

where the $\mathcal{S}$-operator is defined as

$$\mathcal{S} := \mathcal{U}(t)\mathcal{U}^\dagger(t')\,. \tag{2.7}$$

With this definition and using the completeness of the orthogonal eigenstates of $\mathcal{H}$, we can express the wave function of the particle in the Schrödinger picture and in the space time coordinates (x,t) via its value at some previous space-time point (x',t') as

$$\begin{aligned}\psi(x,t) &= \langle x|\phi(t)\rangle = \langle x|\mathcal{S}(t,t')|\phi(t')\rangle \\ &= \int dx' \,\langle x|\mathcal{S}(t,t')|x'\rangle \,\langle x'|\phi(t')\rangle \\ &= \int dx' \,\langle x|\mathcal{S}(t,t')|x'\rangle \,\psi(x',t')\,.\end{aligned} \tag{2.8}$$

By comparing Equation (2.8) with Equation (2.2), we can identify the previously defined propagator

$$K(x,t;x',t') = \langle x|\mathcal{S}(t,t')|x'\rangle\ . \tag{2.9}$$

The Green's function will be the key component for describing a many particle system. Unfortunately, we cannot work with the simple one-particle wave func-

tion any more, but rather need to take the whole many particle wave function into account, which can be expressed by the eigenfunctions of the single particle Hamiltonian. Further, we have to obey the principle of indistinguishable particles, which means by exchanging two particles, the wave function must stay the same modulo a phase factor. The phase factor only takes the values $+1$ or -1, for bosons and fermions respectively. Therefore, a multi-particle wave function must be symmetric (bosons) or antisymmetric (fermions) with respect to particle exchange. The wave function is now a state in Fock space and second quantization operators are acting in it. All operators can be represented by creation/annihilation operators where we distinguish again between bosonic and fermionic ones. We briefly remind here the most important operator relations. In general, the following applies when creation and annihilation operators act on states

$$\psi_i^\dagger \left|\ldots, N_i, \ldots\right\rangle \propto \left|\ldots, N_i + 1, \ldots\right\rangle \tag{2.10a}$$

$$\psi_i \left|\ldots, N_i, \ldots\right\rangle \propto \left|\ldots, N_i - 1, \ldots\right\rangle \,. \tag{2.10b}$$

The field operators $\psi_i^\dagger$ and ψ_i are the creation and annihilation operators for the i-th state respectively and N_i denotes the number of particles in this state. If we consider fermions, N_i can only be 0 or 1, due to the Pauli principle and for bosons N_i can be any positive integer including zero. For the fermionic creation and annihilation operators $c_i^\dagger$ and c_i, one can derive then the anti-commutator relations

$$\left\{c_{i,\sigma}, c_{j,\sigma'}^\dagger\right\} = \delta_{\sigma\sigma'}\delta_{ij} \tag{2.11a}$$

$$\left\{c_{i,\sigma}, c_{j,\sigma'}\right\} = \left\{c_{i,\sigma}^\dagger, c_{j,\sigma'}^\dagger\right\} = 0\,, \tag{2.11b}$$

where the index σ is denoting the spin. The bosonic operators obey the commutator relations

$$\left[b_{i,\sigma}, b_{j,\sigma'}^\dagger\right] = \delta_{\sigma\sigma'}\delta_{ij} \tag{2.12a}$$

$$\left[b_{i,\sigma}, b_{j,\sigma'}\right] = \left[b_{i,\sigma}^\dagger, b_{j,\sigma'}^\dagger\right] = 0\,. \tag{2.12b}$$

By looking back at the propagator and Green's function definition in Equations (2.4) and (2.9), one can formulate the causal Green's function with the general creation

and annihilation operators from Equation (2.10) as

$$\begin{aligned} G_{\boldsymbol{x}\boldsymbol{x}',tt',\sigma\sigma'} &= -i\left\langle \psi_{\boldsymbol{x},t,\sigma}\psi^{\dagger}_{\boldsymbol{x}',t',\sigma'}\right\rangle \Theta(t-t') \mp i\left\langle \psi^{\dagger}_{\boldsymbol{x}',t',\sigma'}\psi_{\boldsymbol{x},t,\sigma}\right\rangle \Theta(t'-t) \\ &= i\left\langle \mathcal{T}\psi_{\boldsymbol{x},t,\sigma}\psi^{\dagger}_{\boldsymbol{x}',t',\sigma'}\right\rangle . \end{aligned} \tag{2.13}$$

In the first line we ensured the causality with the Heaviside function, which was simplified in the last line with the Wick time ordering operator. As one can see, the above definition in Equation (2.13) can be interpreted as the following: a particle with spin σ at position x and time t is annihilated and created at different position x' and time t' with spin σ'. Thus, a propagation. The brackets $\langle\cdots\rangle$ are denoting the Green's function's statistical average over all states of the many-body system, which is its trace with the density operator ρ. In general, for an operator $\mathcal{O}$ this is

$$\langle\mathcal{O}\rangle = \frac{1}{\mathcal{Z}}\mathrm{tr}\left\{\rho\mathcal{O}\right\} = \frac{1}{\mathcal{Z}}\mathrm{tr}\left\{e^{-\beta\mathcal{H}}\mathcal{O}\right\} \tag{2.14a}$$

$$\mathcal{Z} = \mathrm{tr}\left\{\rho\right\} = \mathrm{tr}\left\{e^{-\beta\mathcal{H}}\right\} , \tag{2.14b}$$

where $\mathcal{Z}$ is the partition function of a canonical system. However, we will use the grand canonical formulation of Equation (2.14), where the density operator changes to

$$\rho = e^{-\beta(\mathcal{H}-\mu\mathcal{N})} . \tag{2.15}$$

In this ensemble the exchange of particles is allowed, which is controlled by the chemical potential μ coupling to the particle operator $\mathcal{N}$. For an unperturbed system with Hamiltonian $\mathcal{H}_0$ at zero temperature, one can derive the result for the Fourier transformed causal fermionic Green's function analytically by taking the limit $\beta\to\infty$ and tracing over the eigenstates, which gives

$$\mathcal{G}_{\boldsymbol{k},\omega} = \frac{1}{\omega-(\epsilon_{\boldsymbol{k}}-\mu)+i\mathrm{sgn}(\omega)0^{+}} . \tag{2.16}$$

In the above result, $\epsilon_{\boldsymbol{k}}$ is the dispersion relation and ω the energy. If we want to describe realistic systems, we need a more sophisticated formalism, also taking interactions and finite temperatures into account. This will be the well-known Feynman perturbation theory. The beauty of this theory lies in the fact, that the perturbation is expanded as a series, where each term can be represented as a set

of graphs, the Feynman diagrams. Let us assume we can write the Hamiltonian of the interacting system as

$$\mathcal{H} = \mathcal{H}_0 + \mathcal{W}(t)\,, \tag{2.17}$$

with $\mathcal{W}(t)$ a small time dependent perturbation. This allows us to use the interaction picture, where an operator is defined as

$$\mathcal{A}_{\mathrm{I}}(t) := e^{\frac{i}{\hbar}\mathcal{H}_0 t}\mathcal{A}e^{-\frac{i}{\hbar}\mathcal{H}_0 t}\,. \tag{2.18}$$

From here on, all operators are defined in the interaction picture, including the Green's function which we formulate by using the $\mathcal{S}$-operator, introduced earlier. Further we assume that the adiabatic theorem holds, which leads to the formulation

$$iG_{\boldsymbol{x}\boldsymbol{x}',tt',\sigma\sigma'} = \frac{\langle\Phi_0|\mathcal{T}\mathcal{S}(\infty,-\infty)\Psi_{\boldsymbol{x},t,\sigma}\Psi^{\dagger}_{\boldsymbol{x}',t',\sigma'}|\Phi_0\rangle}{\langle\Phi_0|\mathcal{S}(\infty,-\infty)|\Phi_0\rangle}\,, \tag{2.19}$$

The state $|\Phi_0\rangle$ is the ground state of the unperturbed system and the $\mathcal{S}$-operator is defined in the interaction picture as

$$\mathcal{S}(t,t') = \mathcal{T}e^{-i\int_{t'}^{t}d\bar{t}\mathcal{W}(\bar{t})}\,. \tag{2.20}$$

We mentioned before, that Feynman perturbation theory uses expansion series, in particular the expansion of the exponent in Equation (2.20). One obtains then terms of the form

$$\langle\Phi_0|\mathcal{T}\mathcal{W}(t_1)\mathcal{W}(t_2)\cdots\mathcal{W}(t_n)\Psi_{\boldsymbol{x},t,\sigma}\Psi^{\dagger}_{\boldsymbol{x}',t',\sigma'}|\Phi_0\rangle\,. \tag{2.21}$$

Cutting off at a certain order n and plugging it back in into Equation (2.19) yields the approximation of order n of the interacting Green's function. Each term of this perturbation series consists of multiple operators and can be very complicated. However, with Wick's theorem (see Section 2.1.3) we can reduce the correlation function into sum of non-interacting Green's functions and construct the Feynman diagrams from it.

2.1.2. Matsubara Green's Functions

In the previous derivations, we were working with the system at zero temperature. We now generalize to finite temperature, which means that we have to average over all excited states and not only the ground state. The states are then highly degenerate, the adiabatic theorem is not valid any more and the previous scheme breaks down. However, one can exploit the analogy between the time evolution operator $\exp(-i\mathcal{H}t)$ and the density operator $\exp(-\beta\mathcal{H})$. We define the transformation into imaginary time through the Wick rotation

$$t \leftrightarrow -i\tau\,, \tag{2.22}$$

with $0 < \tau < \beta$. From this definition, one obtains an equation similar to the Schrödinger equation

$$i\frac{\partial}{\partial t}\rho(it) = \mathcal{H}\rho(it)\,. \tag{2.23}$$

As we discussed before, we can use Green's functions to solve the Schrödinger equation. This motivates the definition of the new temperature- or Matsubara Green's function

$$G_{\boldsymbol{x}_1\boldsymbol{x}_2,\tau_1\tau_2,\sigma_1\sigma_2} = -\left\langle \mathcal{T}_\tau \psi_{\boldsymbol{x}_1,\tau_1,\sigma_1}\psi^\dagger_{\boldsymbol{x}_2,\tau_2,\sigma_2}\right\rangle\,. \tag{2.24}$$

The creation and annihilation operator above are the Wick rotated operators

$$\psi_{\boldsymbol{x},\tau,\sigma} = e^{\mathcal{H}\tau}\psi_{\boldsymbol{x},\sigma}e^{-\mathcal{H}\tau} \tag{2.25a}$$

$$\psi^\dagger_{\boldsymbol{x},\tau,\sigma} = e^{\mathcal{H}\tau}\psi^\dagger_{\boldsymbol{x},\sigma}e^{-\mathcal{H}\tau}\,, \tag{2.25b}$$

where the operator $\exp(\mathcal{H}\tau)$ determines the time evolution in imaginary time. Further, the time ordering operator $\mathcal{T}_\tau$ orders now the imaginary time arguments. Let us now explore some important properties of the temperature Green's function. Looking back at the definition in Equation (2.24) of the imaginary time Green's function, one can show by using the cyclic invariance of the trace that the imaginary-time Green's function only depends on the difference $\tau = \tau_2 - \tau_1$, which is valid for any temperature Green's function. We also assume an isotropic system, where the Green's function spatially depends only on the difference $\boldsymbol{x} = \boldsymbol{x}_2 - \boldsymbol{x}_1$.

We can write then

$$G_{\boldsymbol{x}_1\boldsymbol{x}_2,\tau_1\tau_2,\sigma_1\sigma_2} = G_{\boldsymbol{x},\tau,\sigma_1\sigma_2}\,. \tag{2.26}$$

A closer look at Equation (2.32) also reveals why we restricted the imaginary time range to $0 < \tau_{1/2} < \beta$. The reason is, if $\beta < |\tau|$, the sign in the exponent of $\exp\left(\mathcal{H}(\tau - \beta)\right)$ would get positive and the Green's function would diverge. The divergence results from the fact, that there is only a lower bound for the eigenvalues of hermitian operators and the eigenvalues can get arbitrarily big. These two properties, the restriction of the τ-range and that the Green's function only depends on a single τ value, has some further consequences: τ only varies from $-\beta$ to β and therefore can be expanded as the Fourier series with a single set of discrete frequencies ν_n

$$G_{\boldsymbol{x},\tau,\sigma_1\sigma_2} = \frac{1}{\beta}\sum_{n=-\infty}^{\infty} G_{\boldsymbol{x},\nu_n,\sigma_1\sigma_2} e^{-i\nu_n\tau}\,, \tag{2.27}$$

where the frequencies are known as Matsubara frequencies and satisfy

$$\nu_n = \frac{\pi n}{\beta}\,. \tag{2.28}$$

By Fourier transforming this expression in x and ν_n, we obtain the Green's function in k-space and Matsubara frequencies. Hence,

$$G_{\boldsymbol{k},\nu_n} = \int_0^\beta d\tau e^{i\nu_n\tau} G_{\boldsymbol{k},\tau}\,. \tag{2.29}$$

When investigating the periodicity of the Green's function, it can be shown (again by using the cyclic invariance of the trace), that it fulfills

$$G_{\boldsymbol{x},\tau+\beta,\sigma_1\sigma_2} = \mp G_{\boldsymbol{x},\tau,\sigma_1\sigma_2}\,. \tag{2.30}$$

The sign depends on the type of operators used, for fermions it is negative and for bosons positive. It is caused by the exchange of fermionic or bosonic operators and therefore, depends on the statistics. Hence, bosonic(fermionic) Green's functions are (anti-)periodic and only even(odd) coefficients in the Fourier series are non-zero. This allows us to distinguish between the fermionic (ν_n^{F}) and bosonic (ν_n^{B})

Matsubara frequencies

$$\nu_n^{\mathrm{F}} = \frac{(2n+1)\,\pi}{\beta} \tag{2.31a}$$

$$\nu_n^{\mathrm{B}} = \frac{2n\pi}{\beta}\,. \tag{2.31b}$$

We will derive an important representation of the Green's function, the spectral representation. Let us assume we have a Hamiltonian $\mathcal{H}$, whose eigenstates are $|n\rangle$ and E_n the corresponding eigenvalues. We can write the Green's function in k-space and imaginary time as

$$G_{\boldsymbol{k},\tau} = -\frac{1}{\mathcal{Z}}\mathrm{tr}\left\{e^{-\beta\mathcal{H}}e^{\mathcal{H}\tau}c_{\boldsymbol{k}}e^{-\mathcal{H}\tau}c_{\boldsymbol{k}}^{\dagger}\right\}\,. \tag{2.32}$$

After explicitly writing out the trace with a sum, doing the Fourier transformation in Equation (2.29) and inserting a complete set of eigenstates, we get

$$\begin{aligned} G_{\boldsymbol{k},\nu_n} &= -\frac{1}{\mathcal{Z}}\int_0^{\beta} d\tau e^{i\nu_n\tau}\sum_{nm}\langle m|e^{-\beta\mathcal{H}}e^{\tau\mathcal{H}}c_{\boldsymbol{k}}|n\rangle\,\langle n|e^{-\tau\mathcal{H}}c_{\boldsymbol{k}}^{\dagger}|m\rangle \\ &= \frac{1}{\mathcal{Z}}\sum_{nm}e^{-\beta E_m}\frac{\langle m|c_{\boldsymbol{k}}|n\rangle\,\langle n|c_{\boldsymbol{k}}^{\dagger}|m\rangle}{i\nu_n-(E_n-E_m)}e^{i\nu_n\tau-\tau(E_n-E_m)}\Big|_0^{\beta} \\ &= \frac{1}{\mathcal{Z}}\sum_{nm}e^{-\beta E_m}\frac{\pm e^{(-E_n+E_m)\beta}-1}{i\nu_n\underbrace{-E_n+E_m}_{-\omega'}}\,\langle m|c_{\boldsymbol{k}}|n\rangle\,\langle n|c_{\boldsymbol{k}}^{\dagger}|m\rangle\,. \end{aligned}$$

Let us define the spectral function as

$$A_{\boldsymbol{k},\omega'} := \frac{1}{\mathcal{Z}}\left(1\pm e^{-\beta\omega'}\right)\sum_{nm}e^{-\beta E_m}\,\langle m|c_{\boldsymbol{k}}|n\rangle\,\langle n|c_{\boldsymbol{k}}^{\dagger}|m\rangle\,\delta\left(\omega'-(E_n-E_m)\right)\,, \tag{2.33}$$

which allows us to write the Matsubara Green's function in the form

$$G_{\boldsymbol{k},\nu_n} = \int d\omega'\frac{A_{\boldsymbol{k},\omega'}}{i\nu_n-\omega'}\,. \tag{2.34}$$

The result in Equation (2.34) is important and has some physical meaning. If we consider the limits for $T=0$ ($\beta\to\infty$) and positive energy $\omega>0$, the spectral

function becomes

$$A_{\boldsymbol{k},\omega} = \sum_m \left|\langle m|c_{\boldsymbol{k}}|\phi_0\rangle\right|^2 \delta\left(\omega - (E_0 - E_m)\right) . \tag{2.35}$$

This expression tells us the probability of adding or removing a particle with momentum $\boldsymbol{k}$ from the ground state $|\phi_0\rangle$ and adding the energy $-\omega$. Experimentally, this can be realized in photoemission spectroscopy. Equation (2.34) is a relation connecting the Green's function on the imaginary frequency axis with the spectrum on the real axis, through a kernel

$$K_{\nu_n,\omega} = \frac{1}{i\nu_n - \omega} , \tag{2.36}$$

which can also be formulated for imaginary time by doing a Fourier transformation.

Another important property of the Green's function can be derived from the fact, that in general it is a complex function and can be written as a sum of a real and an imaginary part. Because of the analytical properties of the retarded and advanced Green's function, in particular that the causality relation holds, these two parts are not independent from each other. This is described with the Kramers-Kronig relations

$$\begin{aligned} \Re G^{\mathrm{R,A}}_{\boldsymbol{k},\omega} &= \mathcal{P}\frac{1}{\pi}\int d\omega' \frac{\Im G^{\mathrm{R,A}}_{\boldsymbol{k},\omega'}}{\omega - \omega'} \\ \Im G^{\mathrm{R,A}}_{\boldsymbol{k},\omega} &= -\mathcal{P}\frac{1}{\pi}\int d\omega' \frac{\Re G^{\mathrm{R,A}}_{\boldsymbol{k},\omega'}}{\omega - \omega'} . \end{aligned}$$

The operator $\mathcal{P}$ denotes the principle value. Comparing this to Equation (2.34), one also obtains the relation

$$A_{\boldsymbol{k},\omega} = -\frac{1}{\pi}\Im G_{\boldsymbol{k},\omega'} . \tag{2.38}$$

Therefore, the imaginary part of the Green's function has the very important physical meaning of describing the excitation spectrum of the system. We mentioned the spectral function in the previous part, where the mapping onto the real axis is done with the integral in Equation (2.34). However, the kernel for bosonic response functions $\chi_{\boldsymbol{q},\omega}$ is singular at $\omega = 0$. In order to avoid the singularity, we can

define a new function $B_{\boldsymbol{q},\omega}$ and analytic continue it with a different kernel. The starting point is the relation

$$\chi'_{\boldsymbol{q},\omega} = \frac{1}{\pi} \int_{-\infty}^{\infty} d\omega' \frac{\chi''_{\boldsymbol{q},\omega'}}{\omega' - \omega} \tag{2.39}$$

from linear response theory, where we denoted $\chi'_{\boldsymbol{q},\omega}$ as the real part and $\chi''_{\boldsymbol{q},\omega}$ as the imaginary part. Due to causality, one can show that for bosonic response functions $\chi''_{\boldsymbol{q},-\omega} = -\chi''_{\boldsymbol{q},\omega}$ holds. By using this relation on the split up integral (from $-\infty$ to 0 and from 0 to ∞) and dividing the nominator and denominator by ω', Equation (2.39) can be written as

$$\chi'_{\boldsymbol{q},\omega} = \frac{2}{\pi} \int_{0}^{\infty} d\omega' \frac{\omega'^2}{\omega'^2 + \omega^2} \underbrace{\frac{\chi''_{\boldsymbol{q},\omega'}}{\omega'}}_{B_{\boldsymbol{q},\omega'}} . \tag{2.40}$$

This expression will be used in the maximum entropy method, described in Section 2.6.1 for bosonic correlations such as the spin susceptibility.

2.1.3. Wick's theorem

Wick's theorem is one of the most important theorems in quantum field theories. It states that[54] the time-ordered product of field operators in interaction representation equals to the sum of their normal-ordered products with all possible contractions

$$\begin{aligned} \mathcal{T}\psi_1\psi_2\cdots\psi_n =& N\left[\psi_1\cdots\psi_n\right] + \sum_{(ij)} N\left[\psi_1\cdots\overbrace{\psi_i\cdots\psi_j}\cdots\psi_n\right] \\ &+ \sum_{(ij)(kl)} N\left[\psi_1\cdots\overbrace{\psi_i\cdots\overbrace{\psi_k\cdots\psi_j}\cdots\psi_l}\cdots\psi_n\right] \\ &+ \dots , \end{aligned} \tag{2.41}$$

where N denotes normal ordering and the over-braces the pair contractions. The indices in (i, j) denote the summation over pairs. The ψ_i can be creation or annihilation operators and the index i labels any dependency (e.g. time, position, spin).

The normal ordering $N[\psi_1 \cdots \psi_n]$ of some operators means, that all annihilation operators stay on the right of the creation ones. A contraction of two operators is defined as the difference between their time ordered and normal ordered product

$$\overbrace{\psi_i \psi_j} := \mathcal{T}\psi_i\psi_j - N[\psi_i\psi_j] \ . \tag{2.42}$$

Contractions of operators of the same sort (i.e. both annihilation or both creation) vanish, which can be shown by inserting into Equation (2.42). However, contracting two conjugated operators will give a number and can be expressed as an unperturbed Green's function. We are ready to apply the theorem on an example. A simple example, which can be found in Zagoskin[2], is the interaction with strength U of two electrons. Given the perturbation $\mathcal{W}(t)$ of this problem, the first step is to expand the interacting Green's function. If we limit the expansion to first order, we obtain

$$iG_{XX'} \approx \frac{\langle\phi_0|\psi_X\psi^\dagger_{X'}|\phi_0\rangle - \frac{i}{2\hbar}\int\int d1d2U_{12}\,\langle\phi_0|\mathcal{T}\psi^\dagger_1\psi^\dagger_2\psi_2\psi_1\psi_X\psi^\dagger_{X'}|\phi_0\rangle}{1 - \frac{i}{2\hbar}\int\int d1d2U_{12}\,\langle\phi_0|\mathcal{T}\psi^\dagger_1\psi^\dagger_2\psi_2\psi_1|\phi_0\rangle}\,, \tag{2.43}$$

where the 1 and 2 are denoting internal vertices, which will be integrated out. The labels X and X' are carrying the actual significant coordinates of the approximated interacting Green's function. The interaction term U_{12} is acting between the two vertices 1 and 2. In order to find the contributions for the Green's function we need to know another theorem, the linked cluster theorem. It states that we can omit the denominator in Equation (2.43) and at the same time ignore the contributions of disconnected diagrams. When applying Wick's theorem on the correlators in Equation (2.43), one obtains product of non-interacting Green's functions of the form

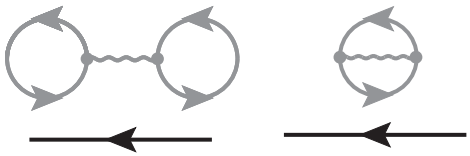

The gray diagrams are called disconnected and only contribute to the vacuum amplitude. Therefore, they cancel with the denominator and we only need to include the connected diagrams. When doing so the only diagrams left in first

order are

$$\mathcal{G}_{XX'} + \mathcal{G}_{X2}\mathcal{G}_{21}\mathcal{G}_{1X'}U_{12} + \mathcal{G}_{X1}\mathcal{G}_{1X'}\mathcal{G}_{22}U_{12} \tag{2.44}$$

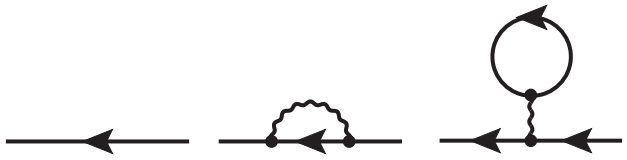

which are the non-interacting Green's function, the Fock term and the Hartree term respectively. As one can see, this method is very powerful and helps to interpret even complicated correlation functions. For more details about Feynman diagrams, we refer to the literature[23, 10, 2].

2.1.4. Self Energy

The self energy is a concept to summarize Feynman diagrams in a compact form and allows it to connect the non-interacting Green's function with the interacting one. This connection is given by the Dyson equation

$$G_{ij,\tau} = \mathcal{G}_{ij,\tau} + \sum_{i'j'} \int_0^\beta \int_0^\beta d\tau' d\tau'' \mathcal{G}_{ii',\tau'} \Sigma_{(i'j',\tau''-\tau')} G_{j'j,\tau''} \tag{2.45}$$

The self energy Σ contains all one-particle irreducible Feynman diagrams, which means, that by cutting one Green's function line, the diagram cannot be separated into two parts. Two of such first-order diagrams, we obtained already in Equation (2.44). However, the self energy usually contains also higher order diagrams and from all the diagrams in the self energy, one can build then all possible reducible contributions to the interacting Green's function. This is essential done in the recursion of Equation (2.45). An example of two second-order reducible diagrams build from the first-order irreducible diagrams in Equation (2.44) are

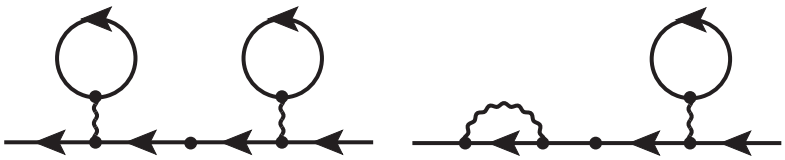

By writing out the recursion, one can build a geometric series from it. Fourier transformed self energy in Matsubara frequencies and in k-space is diagonal and then we can write

$$\begin{aligned} G_{\boldsymbol{k},\nu_n} &= \mathcal{G}_{\boldsymbol{k},\nu_n} + \mathcal{G}_{\boldsymbol{k},\nu_n}\Sigma_{\boldsymbol{k},\nu_n}\mathcal{G}_{\boldsymbol{k},\nu_n} + \mathcal{G}_{\boldsymbol{k},\nu_n}\Sigma_{\boldsymbol{k},\nu_n}\mathcal{G}_{\boldsymbol{k},\nu_n}\Sigma_{\boldsymbol{k},\nu_n} + \dots \\ &= \mathcal{G}_{\boldsymbol{k},\nu_n}\sum_{m=0}^{\infty}\left(\Sigma_{\boldsymbol{k},\nu_n}\mathcal{G}_{\boldsymbol{k},\nu_n}\right)^m \\ &= \mathcal{G}_{\boldsymbol{k},\nu_n}\left(1-\mathcal{G}_{\boldsymbol{k},\nu_n}\Sigma_{\boldsymbol{k},\nu_n}\right)^{-1} = \left(\left[\mathcal{G}_{\boldsymbol{k},\nu_n}\right]^{-1} - \Sigma_{\boldsymbol{k},\nu_n}\right)^{-1}, \end{aligned}$$

and further

$$G^{-1}_{\boldsymbol{k},\nu_n} = \mathcal{G}^{-1}_{\boldsymbol{k},\nu_n} - \Sigma_{\boldsymbol{k},\nu_n} \tag{2.46}$$

The curly $\mathcal{G}$ is denoting the non-interacting Green's function and Σ the self energy. For a detailed discussion of the self energy we refer to the literature[23, 10, 2].

2.2. The Hubbard Model

With the development of quantum theories the necessary tools for describing microscopic effects in materials were given. Scattering experiments showed that the atoms in a solid are arranged in a periodic pattern and upon this, Felix Bloch showed[6] that the wave functions of electrons inside a periodic potential satisfy the same periodicity. His famous theorem was the basis of the first descriptions of metals and their electronic properties. Because of the vast amount of particles in a solid, approximations must be used to solve the underlying Schrödinger equation. A very rudimentary approximation is neglecting the electronic interactions completely and treating the electrons as freely moving inside the potentials of the nuclei. Although, this seems to be a very bad approximation, because the Coulomb interaction is long ranged and every electron should feel all other electrons, it works quite well for certain material types, especially partially filled s and p materials such as for the semiconductor industry important elements Sili-

con, Germanium etc. and corresponding alloys. We call the theory for such weakly correlated materials Fermi liquid theory[1].

Consider a free electron gas where we slowly turn on interactions. If this turning on is slow enough we are in the adiabatic regime and spin, charge and momentum are unchanged. Only dynamical properties such as the mass change to a renormalized value. Therefore, there is a one to one correspondence between elementary excitations in the Fermi gas and Fermi liquid called quasi-particles. Quasi particles can be understand as a collective phenomena e.g a "dressed" electron which is screened from the surrounding electrons. Usually, simple mean field theories are enough for describing weakly correlated materials. If orbitals are getting very narrow, the Coulomb interaction is not screened well any more and the Fermi liquid theory breaks down. This is the case for d and f orbitals. Thus, correlation effects cannot be neglected and a much more difficult problem needs to be solved. The most common model to study such systems is the Hubbard model[8]. We start with the general form of an interacting Hamiltonian and explain the approximations yielding the Hubbard model. The d and f electrons are more localized compared to the s and p electrons and therefore, it is convenient to use the tight-binding representation[49]. The orbital resolved full solid state Hamiltonian with Coulomb interaction and tight-binding approximation in second quantization is

$$\begin{aligned}\mathcal{H} = &\underbrace{-\sum_{ij,mn,\sigma} t_{ij}^{mn} c_{i,m,\sigma}^{\dagger} c_{j,n,\sigma} + \sum_{i,mn,\sigma} \delta_{ij}\delta_{mn}\mu c_{i,m,\sigma}^{\dagger} c_{i,n,\sigma}}_{\mathcal{H}_{\text{hop}}} + \\ &\underbrace{\sum_{\sigma,\sigma',ijkl,mnop} U_{ijkl}^{mnop} c_{i,m,\sigma}^{\dagger} c_{j,n,\sigma'}^{\dagger} c_{k,o,\sigma} c_{l,p,\sigma'}}_{\mathcal{H}_{\text{Int}}},\end{aligned} \tag{2.47}$$

where $\{i, j, k, l\}$ are lattice sites, $\{m, n, o, p\}$ are orbital indices and $\{\sigma, \sigma'\}$ the spins up or down. The hopping term is described through the hopping tensor t_{ij}^{mn} or orbital overlap and the chemical potential μ which controls the filling. The tensor U_{ijkl}^{mnop} is the Coulomb interaction between the electrons. The Hamiltonian in Equation (2.47) contains all the energy bands and the full Coulomb interaction. Hence, we have made no approximations yet. To simplify this model and keep the essential physics we have to do make a few approximations:

1. For lower temperatures the interesting physics happens around the Fermi energy, which is why we consider only the bands around the Fermi level. In the later calculations, we focus on a model Hamiltonian which uses one orbital only. Therefore, for the calculations we drop the orbital dependency completely.

2. As already mentioned, we are interested in the physics of d and f electrons, which are very localized in real space. Thus, we restrict ourself to only nearest neighbour hopping and let the sum in the first term of Equation (2.47) run only over the corresponding nearest neighbours denoted as $< ij >$. Further, we neglect inter-orbital hopping and the hopping tensor becomes t_{ij}. If the hopping is uniform, we can also drop the spatial dependence and set it to a constant value t.

3. We simplify the interaction U_{ijkl} by reducing the spacial dependence. The interaction tensor U_{ijkl} consists of three major parts: $U_{ijij} = V_{ij}$ with $i \neq j$ representing the classical electrostatic interaction between electrons on site i and j. $U_{ijji} = J_{ij}$ with $i \neq j$ is the exchange interaction and responsible for ferro- and anti-ferromagnetic coupling. The onsite Coulomb interaction U_{iiii} is the third part and becomes predominant if the overlap between the Wannier functions and correspondingly the V_{ij} and J_{ij} are small. Thus, as another approximation, we use the U_{iiii} only and extract $U = 2U_{iiii}$. This is called Hubbard interaction[8].

By applying all above mentioned approximations, the Hamiltonian in Equation (2.47) reduces to the Hubbard Hamiltonian

$$\mathcal{H}_{\text{Hubbard}} = -t \sum_{\langle i,j\rangle;\sigma=\uparrow\downarrow} c^{\dagger}_{i,\sigma} c_{j,\sigma} + U \sum_{i} n_{i,\uparrow} n_{i,\downarrow} - \mu \sum_{i} \left(n_{i,\uparrow} + n_{i,\downarrow} \right) . \tag{2.48}$$

Depending on the strength of the interaction U, it is possible to distinguish between a metallic or insulating phase. In general, when U/t increases from zero the system undergoes a phase transition known as Mott metal-insulator transition[36]. When $U \gg t$ on average one lattice site holds one electron, charge fluctuations become negligible and the Hubbard model reduces to the Heisenberg model with a antiferromagnetic exchange coupling of $J \approx -4t^2/U$. In contrast when $U/t \ll 1$

the remaining Hubbard model describes a weakly correlated metal and the electrons are de-localized. Although the Hubbard model is a simple model describing electronic correlation in a lattice, it is not a trivial problem to solve and has kept the community busy for decades[35, 41]. From the various methods developed addressing this problem[12, 9], we use the determinant quantum Monte Carlo approach (Section 2.4), directly solving the Hubbard model at finite temperature in real space, and the dynamical mean field theory (Section 2.5), a diagrammatic approach of solving the Hubbard model.

2.3. Kagome Lattice

The Kagome lattice is a highly frustrated lattice which has been studied by various analytical and numerical methods. Frustrated lattices[52] are at the focus of research because they show remarkable collective phenomena, such as fractional particle excitations (which predict emergent magnetic monopoles) and emergent gauge fields[3]. Another interesting property of Kagome lattices are the existence of flat bands. Flat bands describe non dispersive particles and therefore, particles which effectively cannot hop between lattice sites and are purely localized[21, 56].

In Figure 2.1 we show the Kagome lattice, where the dots are the atoms and the lines the bonds in between. The blue rhomboid is the unit cell we chose, where the two vectors $\vec{a}_1$ and $\vec{a}_2$ are the two basis vectors and the three red dots are the atom-basis.

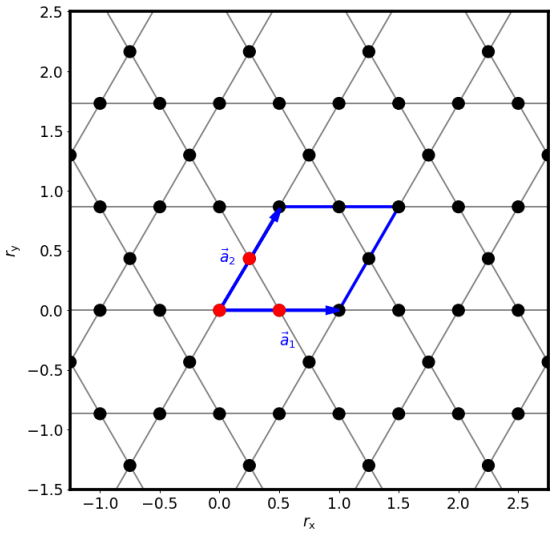

Figure 2.1: The Kagome lattice including a possible unit cell with the two basis vectors in blue and the three basis atoms in red.

The frustration has simple geometric origin: In two dimensions the lattice consists of hexagons and triangles. In order to minimize the total energy, spins of neighbouring lattice sites prefer to align anti-parallel. Due to the triangular motifs in the lattice this is not possible for all neighbouring sites as it can be seen in Figure 2.2.

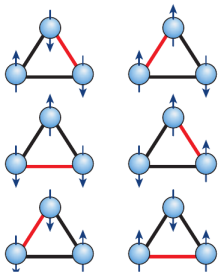

Figure 2.2: Frustration of spin alignment due to geometry[3]. For one triangle there are six possible ground state configurations where black bonds are anti-parallel alignments and red parallel alignments.

As a result a quantum spin liquid is formed in the Heisenberg limit. Here, the constituent spins are correlated and can fluctuate down to very low temperature. This

makes it very challenging to find the minimal energy and the ground state configuration of the system, because it is highly degenerate. Many papers with different methods are published addressing this problem. For example Singh et al.[26, 48] are describing the system as a valence bond crystal (VBC) where two antiparallel lattice sites are forming a valence bond. They developed a series expansion by including five topological graphs of bonds which contribute up to fifth order of perturbation theory. Their result is a VBC consisting of 36 sites per unit cell in a pinwheel distorted lattice. The Kagome lattice was also realized experimentally. A famous example is the mineral Herbertsmithite[37] ($ZnCu_3(OH)_6Cl_2$) which has been synthesised by Shores et al.[47] with copper ions forming a Kagome lattice. Experiments indeed show that there is no ordering of spins down to temperature of 20 mK. Another realization of a Kagome lattice was done by Jo et al.[24] with ultracold atoms. Here, overlaying two commensurate triangular optical lattices give rise to a Kagome lattice.

By looking at the terms in Equation (2.48), we can identify two major parts: the hopping term and the interaction term. If we set $U = 0$, only the hopping term remains and we are able to solve the problem analytically. This is in principle the tight-binding approximation[49, 1] and it only requires to solve the eigenvalue problem. By solving the eigenvalue problem with negative hopping along the high-symmetry points Γ - M - K - Γ, we obtain the band structure in Figure 2.3. By integrating over all k-points we get the non-interacting density of states, shown on the right side. The tight-binding approximation shows us already some important physics:

1. One outstanding feature is the flat band at $\omega = 2$ which appears in the density of states as a delta peak and two Van Hove singularities at $\omega = 0$ and $\omega = -2$ respectively. As mentioned in the introduction, the electrons in the flat band are completely localized, and therefore have infinite effective mass. Of course this is a model Hamiltonian and for a real system the band would not be completely flat. The flat band in Kagome has geometric origins. For other compounds the flat bands appear due to strong electron coupling[39]. Especially compounds containing partially filled $4f$ and $5f$ elements form these bands, and are generally referred to as heavy fermion metals. These compounds are in focus of current research because of interesting properties

such as unconventional superconductivity[27].

2. Another important property, which can directly be see from the non-interacting density of states is that the system is non particle hole symmetric. The non-symmetry only results from the flat band. Without the flat band, only the dispersing bands are left and those are symmetric around $\omega = -1$.

3. The band structure also shows a crossing of bands at the K point. Therefore, in the tight-binding description of electrons on the Kagome lattice yields a metallic behavior.

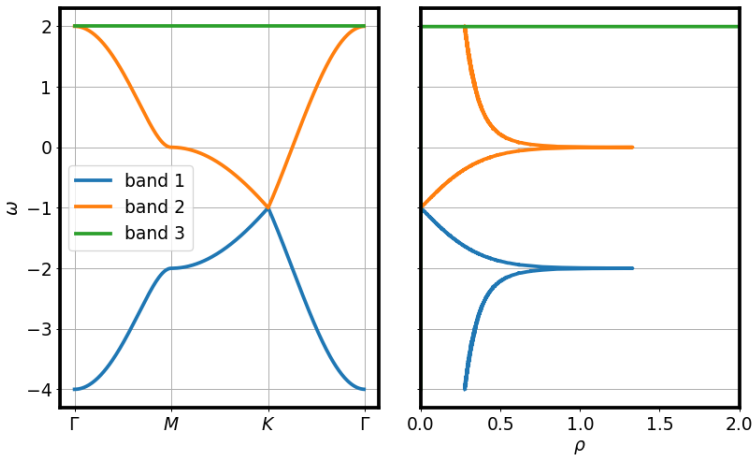

Figure 2.3: The orbital resolved band structure and density of states of the non-interacting case. We used the definition of the hopping term term in Section 2.2 with a leading minus sign. For positive hopping $t = 1$ it gives the above band structure with the flat band on top. For $t = -1$, the flat band would be at the bottom.

2.4. Determinant Quantum Monte Carlo

In order to characterize phase transitions, one would like to know how the system changes under attestation of temperature, interaction strength, doping or other variables. More precisely, one wants to evaluate certain observables characterizing phase transition. In the thermodynamic equilibrium, observables are calculated by summing up the weighted values of the observable on every phase space point. The weight for the sum or integral, depending if the system is discrete or continuous,

is given by a Boltzmann factor. In general we distinguish between microscopic, canonical and grand canonical ensemble. The case we are interested in is the grand canonical ensemble, for which the Hubbard Hamiltonian in Equation (2.48) is defined. The grand canonical ensemble allows exchange of heat and particles for a constant volume. Before we go into detail with the DQMC algorithm, we want to explain why we are able to use only matrices rather than the real Hamiltonians consisting of the fermionic operators. There is a theorem allowing us to only use their matrix representations, which is based upon the fact, that the fermionic operator can be traced out. Consider the Hamiltonian below, consisting of two terms $\mathcal{K}$ and $\mathcal{V}$, which can be expressed as

$$\mathcal{H} \ = \mathcal{K} + \mathcal{V} = \sum_{ij\sigma} c^{\dagger}_{i,\sigma} \left(\underbrace{K_{ij,\sigma} + V_{ij,\sigma}}_{H_{ij,\sigma}} \right) c_{j,\sigma} \, . \tag{2.49}$$

Here, the non-curly operators $K_{ij,\sigma}$, $V_{ij,\sigma}$ and $H_{ij,\sigma}$ denote the matrix representation, which remains after tracing out the fermionic operators. In the following, we will only work with these matrix representations of the original operators.

Let us consider first a classical system, where the thermodynamic weight of a state is given by

$$Z^{-1} e^{-\beta(H-\mu N)} \, . \tag{2.50}$$

and where the partition function is calculated through

$$Z = \int \frac{dp_1 \cdots dp_{3N} dx_1 \cdots dx_{3N}}{h^{3N} N!} e^{-\beta(H(p,q)-\mu N)} \, , \tag{2.51}$$

where q and p denote location and momentum respectively and h is the Planck constant. As it can be seen already, depending on the phase space dimension, the evaluation of this integral can be rather expensive. For such high dimensional integral, Monte Carlo simulations are a perfect numerical fit. We will go now to quantum mechanical systems where the calculation of the partition function Z changes to

$$Z = \mathrm{tr} \left[e^{-\beta(H-\mu N)} \right] = \sum_{n} \langle n | e^{-\beta(H-\mu N)} | n \rangle \ , \tag{2.52}$$

and the statistical average of an operator O is given by

$$\langle O \rangle = \mathrm{tr}\left[e^{-\beta(H-\mu N)}O\right] , \tag{2.53}$$

in analogy to the operators in Equation (2.14). If we now assume a system with N particles, the sum in Equation (2.53) consists of 4^N summands. Therefore, is of order $\mathcal{O}(4^N)$ and has exponential complexity. Directly evaluating such a trace is even for small systems numerically not favourable. However, it is possible to relate the trace to calculating a determinant through[5]

$$\mathrm{tr}\left[e^{-\beta(H-\mu N)}\right] = \det\left[1 + e^{-\beta(H-\mu N)}\right] . \tag{2.54}$$

This expression is an identity if the Hamiltonian has a quadratic form. Numerically, the calculation of the determinant of a general matrix is of order N^3 and therefore, a major gain compared to the 4^N order of the trace. This relation will be the central idea of the determinant quantum Monte Carlo method. But before this equation will be of any use, some further steps have to be done, which are described in the following sections.

2.4.1. Trotter decomposition

To calculate a statistical average by the method described in the previous section, we first have to take a look at properties of the Hamiltonian. If we consider a Hubbard Hamiltonian, it can be split up into an hopping H_{hop} and interaction part H_{int}.

$$H = \underbrace{-t \sum_{<ij>,\sigma} c^{\dagger}_{i,\sigma} c_{j,\sigma} + \mu \sum_{i} \left(n_{i,\uparrow} + n_{i,\downarrow}\right)}_{H_{\mathrm{hop}}} + \underbrace{U \sum_{i} n_{i,\uparrow} n_{i,\downarrow}}_{H_{\mathrm{int}}} . \tag{2.55}$$

The hopping term is modeled by the inter-orbital hopping with constant hopping parameter t and constant chemical potential μ as described in Section 2.2. The separation between the hopping and interaction part is necessary to distinguish between quadratic and quartic fermionic terms, because the quartic term needs an additional treatment, which will be a Hubbard-Stratonovich transformation. It is

helpful to split up the exponential term into successive small pieces in order to be able to evaluate imaginary time propagation. Thus,

$$e^{-\beta H} = \prod_{m}^{L} e^{-\Delta\tau K} e^{-\Delta\tau V} + \mathcal{O}\left((\Delta\tau)^2\right) , \tag{2.56}$$

where $\Delta\tau L = \beta$. The Hamiltonian parts K and V are possible not commuting and therefore, one makes an error of order $tU\left(\Delta\tau\right)^2$, known as Trotter error. Because of this error scaling, it is important to carefully choose the number of time slices L and the $\Delta\tau$. A rule of thumb is to to keep $\Delta\tau$ below $1/10$ and thus have $tU\left(\Delta\tau\right)^2 << 1$. However, if one is interested in the dynamical properties of a correlation, it is better to keep L fixed to have a good resolved imaginary time correlation. In some of the upcoming simulations, we chose a dens time grid with $L = 500$.

2.4.2. Hubbard-Stratonovich Transformation

In the previous section we separated the quartic interaction term from the quadratic interactions. In order to treat the quartic direct electronic interactions, we replace it with a quadratic term coupling to an auxiliary bosonic field. This is called a Hubbard-Stratonovich transformation. Through the Trotter decomposition we get terms such as $\exp\left(-\Delta\tau H_{\text{hop}}\right)\exp\left(-\Delta\tau U n_{i,\uparrow} n_{i,\downarrow}\right)$ where we can completely separate the hopping term from the interaction term at each time slice. This allows us to treat the interaction independently. Basically, the Hubbard-Stratonovich transformation is rewriting the quadratic appearance of an operator of an exponential, into a linear one by the cost of introducing a new auxiliary field

$$e^{\frac{1}{2}\hat{A}^2} = \sqrt{2\pi} \int_{-\infty}^{\infty} dx e^{-\frac{1}{2}x^2 - x\hat{A}} , \tag{2.57}$$

where x is the new continuous auxiliary field. The fermions in the quartic term $n_{i\uparrow}n_{i\downarrow}$ in the Hamiltonian can only take the values 0 and 1, we can express the operator $n_{i\uparrow}n_{i\downarrow}$ in terms of the local density $n_i = n_{i\uparrow} + n_{i\downarrow}$ and local magnetization

operator $m_i = n_{i\uparrow} - n_{i\downarrow}$ through

$$n_{i,\uparrow}n_{i,\downarrow} = -\frac{1}{2}m_i^2 \; + \frac{1}{2}n_i \tag{2.58a}$$

$$n_{i,\uparrow}n_{i,\downarrow} = \frac{1}{2}n_i^2 \; - \frac{1}{2}n_i \tag{2.58b}$$

$$n_{i,\uparrow}n_{i,\downarrow} = \frac{1}{4}n_i^2 \; - \frac{1}{4}m_i^2 \; .. \tag{2.58c}$$

The auxiliary field couples then to the local magnetization and local density if the first two Equations (2.58a) and (2.58b) are used. This also leads to a discrete auxiliary field[19] instead of the continuous field in Equation (2.57). The discrete field then only takes the values $s = \pm 1$ and we can do Monte Carlo much like in the classical Ising case by randomly flipping $+1$ to -1 or -1 to $+1$. Finally, we can express the interaction term in the partition function through a coupling of the charge or magnetization to the Hubbard-Stratonovich field. For the repulsive case $U > 0$, Equation (2.58a) is a good choice which allows to rewrite the interaction term as

$$e^{-U\Delta\tau n_{i,\uparrow}n_{i,\downarrow}} = \frac{1}{2}e^{-\frac{U\Delta\tau}{2}n_i}\sum_{s=\pm 1} e^{s\lambda m_i} = \frac{1}{2}\sum_{s=\pm 1}\prod_{\sigma=\uparrow\downarrow} e^{-(\sigma s\lambda + \frac{U\Delta\tau}{2})n_{i,\sigma}} \, , \tag{2.59}$$

where $\cosh\lambda = \exp(1/2|U|\Delta\tau)$. For the attractive case Equation (2.58b) is better and the interaction term becomes

$$e^{|U|\Delta\tau n_{i,\uparrow}n_{i,\downarrow}} = \frac{1}{2}\sum_{s=\pm 1}\prod_{\sigma=\uparrow\downarrow} e^{(s\lambda + \frac{|U|\Delta\tau}{2})(n_{i,\sigma}-\frac{1}{2})} \, . \tag{2.60}$$

Because of the Trotter decomposition, the Hubbard-Stratonovich has also a time dependency. For convenience, we define the time dependent interaction field $V_{i\tau\sigma}$ as

$$V_{i,\tau,\sigma} = \frac{1}{\Delta\tau}\lambda\sigma s_{i,\tau} + \left(\mu - \frac{U}{2}\right) \, , \tag{2.61}$$

where τ is in the discrete case representing the index of the L time slices. By substituting the interaction term in the determinant of Equation (2.54) with Equation (2.60), the determinant will contain matrix products of the form

$$B_{\tau,\sigma} = e^{-\Delta\tau K}e^{-\Delta\tau V_{\tau,\sigma}} \, , \tag{2.62}$$

where B_τ, K and $V_{\tau,\sigma}$ are $N \times N$ matrices, with N the number of sites. It is worth to point out that $V_{\tau,\sigma}$ is diagonal which is why we denoted $V_{i,\tau,\sigma}$ without a second spatial index and the Hubbard-Stratonovich field is a pure local property. Therefore, it is trivial to evaluate the exponent $e^{-\Delta\tau V_{\tau,\sigma}}$ compared to the hopping term.

By applying the Trotter decomposition and using the Hubbard-Stratonovich transformation, we can finally express the partition function as

$$\begin{aligned} Z &= \left(\frac{1}{2}\right)^{N^d L} \sum_{s=\pm 1} \prod_{\sigma=\uparrow\downarrow} \det\left[1 + B_{\beta,\sigma} B_{(\beta-\Delta\tau),\sigma} \dots B_{0,\sigma}\right] \\ &= \left(\frac{1}{2}\right)^{N^d L} \sum_{s=\pm 1} \prod_{\sigma=\uparrow\downarrow} \det\left[\mathcal{O}_\sigma\right] . \end{aligned} \tag{2.63}$$

Above equation is on of the central results for the DQMC.

2.4.3. Simulation

In the previous sections we introduced the fundamental equations behind the DQMC algorithm and how to obtain the partition function. An even more important quantity within the DQMC algorithm is the Green's function, which we will explain how to calculate before we describe the full DQMC algorithm. As we described in Section 2.1 the Green's function can be written as a product of a fermionic creation and annihilation operators, where the equal-time and time dependent Green's functions can be expressed as elements of the matrices

$$G_{ij,\sigma} = \langle c_{i,\sigma} c^\dagger_{j,\sigma} \rangle = \left(\left[1 + B_{\beta,\sigma} B_{(\beta-\Delta\tau),\sigma} \dots B_{0,\sigma}\right]^{-1}\right)_{ij} \tag{2.64a}$$

$$G_{ij,\tau\tau',\sigma} = \langle c_{i,\tau,\sigma} c^\dagger_{j,\tau',\sigma} \rangle = \left[B_{\tau,\sigma} B_{(\tau-\Delta\tau),\sigma} \dots B_{(\tau'+\Delta\tau),\sigma} g_{(\tau'+\Delta\tau),\sigma}\right]_{ij} , \tag{2.64b}$$

with the $B_{\tau,\sigma}$ matrices defined in Equation (2.62) and $g_{\tau,\sigma}$ as the $N \times N$ Green's function matrix at time slice τ and spin σ, defined as

$$g_{\tau,\sigma} = \left[1 + B_{(\tau-\Delta\tau),\sigma} B_{(\tau-2\Delta\tau),\sigma} B_{0,\sigma} B_{\beta,\sigma} \dots B_{\tau,\sigma}\right]^{-1} . \tag{2.65}$$

We are not going to outline the detailed derivation of these equations but want to mention, that the derivation involves a change of the operators representations into the Heisenberg picture and using their diagonal form. After reordering the trace in the thermal brackets, one yields the above result. For more information see the appendix of dos Santos' paper[44].

The DQMC algorithm is similar to the classical Monte Carlo algorithm for Ising spins, but rather by flipping the spins on lattice sites, we flip the Hubbard-Stratonovich field configuration $s_{i,\tau}$ in the space-time lattice and the Boltzmann weight will be calculated differently. As always, the start is to choose an initial configuration, which can be done by either assigning it randomly or using a constant configuration. Next, is to sweep through the space-time lattice, where the start is the first time slice $\tau = 0$ and apply Equation (2.64a) to calculate the Green's function. The algorithm continues by sweeping through the spatial lattice and proposing a move by flipping $s_{i,\tau}$ on a site i. By doing this, the matrices $B_{i,\sigma}$ change to $B'_{i,\sigma}$ through the potential term $V_{ij,\tau,\sigma}(s) \to V_{ij,\tau,\sigma}(-s) = -V_{ij,\tau,\sigma}(s) = V'_{ij,\tau,\sigma}(s)$. For this proposed move we have to calculate then the Boltzmann weight, which is done by building the ratio

$$r' = \frac{\det\left[\mathcal{O}'_{\uparrow}\right]\det\left[\mathcal{O}'_{\downarrow}\right]}{\det\left[\mathcal{O}_{\uparrow}\right]\det\left[\mathcal{O}_{\downarrow}\right]} = \prod_{\sigma=\uparrow,\downarrow} r'_{\sigma}\,, \tag{2.66}$$

with $\mathcal{O}_\sigma$ defined in Equation (2.63) and

$$r'_{\sigma} = \frac{\det\left[\mathcal{O}'_{\sigma}\right]}{\det\left[\mathcal{O}_{\sigma}\right]}\,. \tag{2.67}$$

The above definition of the ratio would require to calculate four determinants, which actually can be avoided by using the Green's function instead. This leads to the expression

$$r'_{\sigma} = 1 + \left(1 - g_{ii,\tau,\sigma}\right)\gamma_{i,\tau,\sigma}\,, \tag{2.68}$$

with the matrix $\gamma_{i,\tau,\sigma} = e^{V_{i,\tau,\sigma}} - 1$, where we used the fact again, that V is diagonal and each spin σ appears at just one element. The probability of accepting a move is then given by $r'/(1+r')$, which is known as the heat-bath algorithm. If the move

is accepted, the new updated Green's function has to be calculated. There are two possibilities, either by calculating the Green's function from scratch through Equation (2.64) or by calculating it from the previous Green's function with

$$g'_{ij,\tau,\sigma} = g_{ij,\tau,\sigma} - \frac{\left(\delta_{ji} - g_{ji,\tau,\sigma}\right)\gamma_{i,\tau,\sigma} g_{ik,\tau,\sigma}}{1 + \left(1 - g_{ii,\tau,\sigma}\right)\gamma_{i,\tau,\sigma}} \,. \tag{2.69}$$

Obviously, the latter one seems favourable in terms of performance, because it scales with $\mathcal{O}(N^2)$. However, it comes with the disadvantage, that by multiple applying Equation (2.69), the error amplifies. To avoid that the Green's function is drifting away to much, it has to be calculated from scratch every once and a while using Equation (2.64). After sweeping through all spacial sites of the $\tau = 0$ time slice, the algorithm starts with the next time slice $\tau = \Delta\tau$ and first spacial site again. As before, the Green's function for the new time slice has to be calculated which can be done from scratch or with the iterative solution

$$g_{(\tau+\Delta\tau),\sigma} = B_{\tau,\sigma} g_{\tau,\sigma} \left[B_{\tau,\sigma}\right]^{-1} \,. \tag{2.70}$$

For the iterative solution, the same $\mathcal{O}(N^2)$ scaling advantage and same error amplifying disadvantage are present. This whole procedure is repeated for every time slice, which then completes the Monte Carlo loop. The Monte Carlo loop itself is then done many times. Before any measurements can be performed, the system has to be brought into equilibrium, which is done by a bunch of warmup sweeps at the beginning of the simulation, where usually a several hundred are enough. After that, the algorithm starts doing measurements, which we describe in Section 2.4.4. However, this only describes a single Monte Carlo simulation and frankly, one cannot obtain reliable data from it. What one has to do is, to run multiple independent simulations from which a statistic can be calculated. Independent means, that the sequence of spin flips between simulations has to be different, which can be achieved e.g. through a different random seed, if pseudo random generators are used. A set of simulations is then called a bin, for which statistics can be calculated with resampling methods. Two famous ones are the bootstrap and jackknife method. In this project we used the jackknife resampling. The first step is to calculate the mean value $\bar{x}_i$ for each subsample i of the set,

by averaging all simulations in the subsample and omitting the i-th simulation. Thus,

$$\bar{x}_i = \frac{1}{N-1} \sum_{j=1, i \neq j}^{N} x_j \,. \tag{2.71}$$

From that, the mean value of the bin is calculated by averaging over all subsample mean values through

$$\bar{x} = \frac{1}{N} \sum_{i=1}^{N} \bar{x}_i \,. \tag{2.72}$$

The jackknife estimate of the variance is then calculated with

$$\mathrm{Var}(\bar{x}) = \frac{N-1}{N} \sum_{i=1}^{N} \left(\bar{x}_i - \bar{x}\right)^2 \,. \tag{2.73}$$

As mentioned in the previous parts, one big disadvantage of QMC methods is the minus sign problem, specially for the DQMC. In DQMC it results from the fact, that apart from some cases, there is no guarantee that the determinant $\det\left[\mathcal{O}_\sigma\right]$ in Equation (2.63) is positive definite.

2.4.4. Measurements

In this section we describe how the measurements in determinant quantum Monte Carlo are performed and we will give some examples. In principle there are time dependent and time independent measurements. Typical time independent measurements are observables such as densities, magnetization but also equal correlation functions e.g. spin-spin correlators in real space or their Fourier transforms (structure factors). The time dependent measurements are dynamical observables where we can also investigate the energy dependency of correlation functions. But to obtain the energy dependency one first has to do a non trivial post processing task, which transforms the observable back onto the real frequency axis, also known as analytic continuationSection 2.6. The central idea of measuring is to reduce the correlator into Green's functions, possible because Wick's theorem holds. The DQMC method allows it to directly sample the single particle Green's function and in combination with Wick's theorem, which was introduced in Sec-

tion 2.1.3, we can measure even complex correlators consisting of many fermionic operator. Examples are the following density-density correlations, consisting of four fermionic operators each.

$$\begin{aligned}
\left\langle n_{i,\sigma} n_{j,\sigma} \right\rangle &= \left\langle c^\dagger_{i,\sigma} c_{i,\sigma} c^\dagger_{j,\sigma} c_{j,\sigma} \right\rangle = \left\langle c^\dagger_{i,\sigma} c_{i,\sigma} \right\rangle \left\langle c^\dagger_{j,\sigma} c_{j,\sigma} \right\rangle && \text{(2.74a)} \\
&+ \left\langle c^\dagger_{i,\sigma} c_{j,\sigma} \right\rangle \left\langle c_{i,\sigma} c^\dagger_{j,\sigma} \right\rangle && \text{(2.74b)} \\
&= \left(1 - G_{ii,\sigma}\right)\left(1 - G_{jj,\sigma}\right) + \left(\delta_{ij} - G_{ji,\sigma}\right) G_{ij,\sigma} \\
\left\langle n_{i,\sigma} n_{j,\bar{\sigma}} \right\rangle &= \left\langle c^\dagger_{i,\sigma} c_{i,\sigma} c^\dagger_{j,\bar{\sigma}} c_{j,\bar{\sigma}} \right\rangle = \left\langle c^\dagger_{i,\sigma} c_{i,\sigma} \right\rangle \left\langle c^\dagger_{j,\bar{\sigma}} c_{j,\bar{\sigma}} \right\rangle && \text{(2.74c)} \\
&= \left(1 - G_{ii,\sigma}\right)\left(1 - G_{jj,\bar{\sigma}}\right)
\end{aligned}$$

We used the Wick's theorem and the anti-commutator relations of the fermionic operators, described in Section 2.1 to represent the pair contractions as equal-time Green's functions. The Wick's theorem is not restricted to equal-time correlation and also works for time dependent correlators. However, for time dependent correlations it is important to use time ordering. One important time dependent correlation function we want to mention here is the susceptibility $\chi^{\mathrm{z}}_{ij,\tau\tau'} = \langle S^{\mathrm{z}}_{i,\tau} S^{\mathrm{z}}_{j,\tau'} \rangle$ of the z-spin component. By expressing this definition of this correlation function in terms of fermionic operators, applying the Wick's theorem again and using Equations (2.74b) and (2.74c) we get

$$\begin{aligned}
\chi^{\mathrm{z}}_{ij,\tau\tau'} &= \Big\langle \mathcal{T}_\tau \underbrace{\left(n_{i,\tau,\sigma} - n_{i,\tau,\bar{\sigma}}\right)}_{S^{\mathrm{z}}_{i,\tau}} \underbrace{\left(n_{j,\tau',\sigma} - n_{j,\tau',\bar{\sigma}}\right)}_{S^{\mathrm{z}}_{j,\tau'}} \Big\rangle \\
&= \left\langle \mathcal{T}_\tau\, n_{i,\tau,\sigma} n_{j,\tau',\sigma} \right\rangle + \left\langle \mathcal{T}_\tau\, n_{i,\tau,\bar{\sigma}} n_{j,\tau',\bar{\sigma}} \right\rangle \\
&- \left\langle \mathcal{T}_\tau\, n_{i,\tau,\bar{\sigma}} n_{j,\tau',\sigma} \right\rangle - \left\langle \mathcal{T}_\tau\, n_{i,\tau,\sigma} n_{j,\tau',\bar{\sigma}} \right\rangle \\
&= \left(G_{ii,\tau\tau,\sigma} - G_{ii,\tau\tau,\bar{\sigma}}\right)\left(G_{jj,\tau'\tau',\sigma} - G_{jj,\tau'\tau',\bar{\sigma}}\right) \\
&- G_{ji,\tau'\tau,\sigma} G_{ij,\tau\tau',\sigma} - G_{ji,\tau'\tau,\bar{\sigma}} G_{ij,\tau\tau',\bar{\sigma}} \\
&+ \delta_{ij}\left(G_{ij,\tau\tau',\sigma} + G_{ij,\tau\tau',\bar{\sigma}}\right) .
\end{aligned} \tag{2.75}$$

This correlator will be especially important for investigating the dynamic magnetic characteristics of the Kagome system e.g the dynamic structure factors.

2.4.5. Checkerboard Approximation

As we previously saw, the calculation of the partition function requires for each spin at least L, probably dense, matrix multiplications and a determinant evaluation. For the Green's function an additional matrix inversion is necessary as well. Further, for each time slice we have to exponentiate the hopping matrix K as outlined in Equation (2.62). Compared to the dens matrix multiplication, scaling with $\mathcal{O}(N^2)$, the exponentiating of K is relatively cheap. Therefore, the biggest bottleneck in performance is the multiplication of dense matrices. This is why we will introduce an additional approximation, called checkerboard approximation, which gets rid of the dense matrices and replaces them with sparse ones, yielding a better scaling in terms of computation time. The starting point is to again split up the exponential much like as in the Trotter approximation. Of course we only want to split up the hopping term, because the potential term is diagonal anyways. Hence,

$$\exp\left(\Delta\tau K\right) = \exp\left(\Delta\tau \sum_n K^{(n)}\right) \approx \prod_n \exp\left(\Delta\tau K^{(n)}\right), \tag{2.76}$$

where the $K^{(n)}$ are strictly sparse matrices with zero diagonal. Constructing the $K^{(n)}$ depends on the geometry and can not be trivial for certain lattices. Lee et. al.[28] are listing some checkerboard break ups for different geometries.

2.4.6. Determining the Chemical Potential

In Chapter 1 and section 2.3 we gave an introduction to the Kagome system and mentioned its properties and relevance. We want to point out that when doing calculation on a system, in particular with the grand canonical Hubbard Hamiltonian described in Section 2.2, one first have to choose a filling by setting the chemical potential μ properly. This is important, because the filling sets the Fermi level at a certain position in the band structure and hence, selects the "types" of electrons contributing in the interaction. The filling corresponds to a density n which can take values between zero and two. The case where $n = 1$, is the case of half filling. For a particle hole symmetric system (e.g. the square lattice) at half filling the chemical potential in Equation (2.48) must be set to zero to get $n = 1$, if convention Equation (2.48) is used. This is not true for non-particle hole symmetric systems such as the Kagome lattice. Therefore, one first has to guess the chemical

potential yielding the filling one wants to have. This can be very tedious if done by hand, which is why we introduce here an iterative scheme to obtain the chemical potential. The scheme is based on the "false position method" or "regular falsi" root finding algorithm. The false position method originally is used to finding roots of functions, but it trivial to altered to find roots on a "shifted" x-axis. In our case, the y-axis is the density n and the x-axis is the chemical potential μ, which is shifted up by the density n_0 one wants to obtain. The algorithm requires to evaluate the function $n(\mu)$ at certain points for which each we ran a Monte Carlo simulation with a small number of warmup and measurement sweeps to avoid a long runtime. This worked surprisingly well, although we only used 100 warmup sweeps and 400 measurement sweeps. The difference of the density from the real simulation is within the Trotter error and therefore neglect-able. The start of the algorithm is to calculate the density for two initial points, where we chose $\mu_0^a = -2$ and $\mu_0^b = 2$. Then, the intersection with the secant of the two points and with $n = n_0$ is calculated through

$$\mu_{\text{int}} = [n_0 - n(b_i)] \cdot \frac{b_i - a_i}{n(b_i) - n(a_i)} + b_i \,. \tag{2.77}$$

The intersection point with $n = n_0$ is one end point of the new secant for the next iteration $i + 1$. Depending which previous secant end point has the opposite sign of $n(\mu_{i+1}) - n_0$, is the other new secant end point. This procedure is repeated until a convergence criteria is reached or an iteration number is exceeded. Figure 2.4 outlines the algorithm in a pseudo function and shows the secants of the first two iterations. Usually, this method converges already within 5 to 10 iterations and thus is very effective for finding the chemical potential.

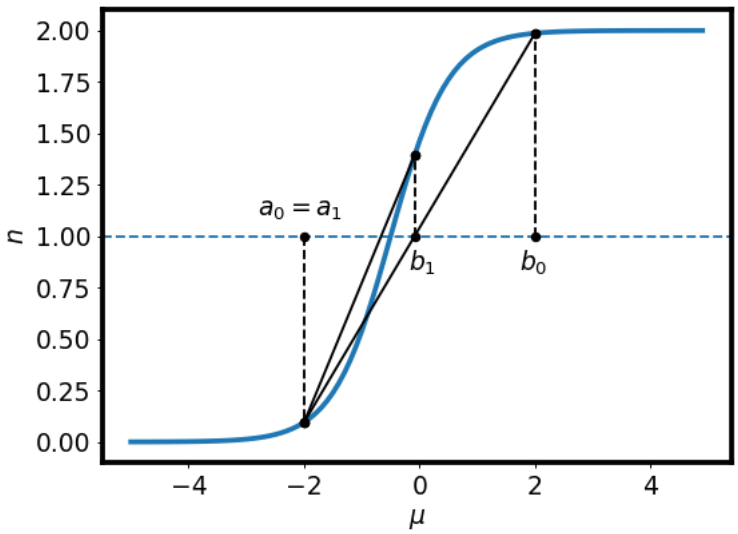

Figure 2.4: Example of false position method showing the secants of the first two iterations.

2.5. Dynamical Mean Field Theory

The dynamical mean field theory (DMFT) is a well established method in the condensed matter theory for dealing with strong electronic correlations. There are many papers and articles describing the method in detail and therefore, in the following only a short overview will be given. For a more detailed description see [13, 18, 42]. To deal with complex problems, it is usually not enough to look at the limits of the non-interacting case or the limit of no kinetic energy, because the interesting physics emerges in the intermediate region between these two limits. There is another limit preserving the interaction strength and kinetic energy but resulting in a momentum independent treatment, which is the $d \to \infty$ limit, the limit of infinite dimensions. This is equivalent to a lattice with infinite coordination number[33, 13]. In this limit, all dynamic correlations are purely local. To really solve the approximation in infinite dimensions, one has to map it first onto an Anderson impurtiy model (AIM) in a self-consistent way. The general AIM in

k-space is

$$\begin{aligned}\mathcal{H}_{\mathrm{AIM}} = &\sum_{\boldsymbol{k},i,\sigma} \epsilon_{\boldsymbol{k},i} a^{\dagger}_{\boldsymbol{k},i,\sigma} a_{\boldsymbol{k},i,\sigma} + \sum_{\boldsymbol{k},i,j,\sigma} \left[V_{\boldsymbol{k},ij} a^{\dagger}_{\boldsymbol{k},i,\sigma} c_{\boldsymbol{k},j,\sigma} + \mathrm{h.c.} \right] \\ &+ \sum_{i,j,l,m,\sigma,\sigma'} U_{ijlm} c^{\dagger}_{i,\sigma} c^{\dagger}_{j,\sigma'} c_{l,\sigma'} c_{m,\sigma} \,.\end{aligned} \tag{2.78}$$

The AIM describes the interaction of a bath of non-interacting electrons with an impurity, represented by the first and second term respectively. The operators $a^{\dagger}_{i,\sigma}$ and $a_{i,\sigma}$ denote the creation and annihilation operators of bath electrons with spin σ, where $c^{\dagger}_{i,\sigma}$ and $c_{i,\sigma}$ are creation and annihilation operators of impurity electrons with spin σ respectively. The bath term describes free electrons with the dispersion relation of $\epsilon_{\boldsymbol{k},i}$, hybridizing with the impurity through a hybridization term $V_{\boldsymbol{k},ij}$. The third term describes the interaction of electrons in the impurity. The DMFT algorithm is a self-consistent scheme, where the self energy from Equation (2.46) plays an important role. All quantities are purely local, which we denote with the superscript "loc". The algorithm goes as follows:

1. A trial self energy is chosen and from which one can calculate the non-interacting Green's function through a reformulation of Equation (2.46). Thus,

$$\mathcal{G}^{\mathrm{loc}}_{\nu_n} = \left(\left[\frac{1}{V_{\boldsymbol{k}}} \int_{\mathrm{BZ}} d\boldsymbol{k} G_{\boldsymbol{k},\nu_n} \right]^{-1} + \Sigma^{\mathrm{loc}}_{\nu_n} \right)^{-1} . \tag{2.79}$$

2. This $\mathcal{G}$ will then be used to calculate the Green's function of the impurity problem Equation (2.78). In this step all irreducible Feynman diagram are constructed with the given $\mathcal{G}$ and U.

3. After the new interacting Green's function G is obtained, a new self energy is calculated through

$$\Sigma^{\mathrm{loc}}_{\nu_n} = \left[\mathcal{G}^{\mathrm{loc}}_{\nu_n} \right]^{-1} - \left[G^{\mathrm{loc}}_{\nu_n} \right]^{-1} . \tag{2.80}$$

4. The new self energy is then plugged in again in step 2, which closes the cycle.

The above steps are repeated until a convergence criteria is reached e.g. $\Sigma^{(n+1)} = \Sigma^{(n)}$. The result is then the solution of the one AIM with an adapted hybridization

$V_{\boldsymbol{k},ij}$, yielding the same solution than the original Hubbard model.

2.6. Analytic Continuation

In Section 2.4 and Section 2.5 we explained two well-known computational methods used to solve the correlated many-body problems by computing the Matsubara Green's functions and through that other dynamical quantities in imaginary time/frequencies can be calculated. In order to compare these results with real experiments, we have to transform it back from imaginary time/frequency into real time/frequency. A common experimental result is the excitation spectrum of a system, which is directly related with the Green's function through Equation (2.38). For transformation of the Matsubara Green's function back onto the real-axis, one has to compute Equation (2.34) by integrating over the kernel in Equation (2.36). However, this is a non-trivial procedure, due to small statistical fluctuations in imaginary space lead to large fluctuations in real space and it is therefore an ill conditioned transformation. The instability of the solution can also be seen when performing a single value decomposition. Let us for now consider the discrete case, where the Green's function and spectral function are vectors and the kernel is a matrix. The analytic continuation problem can then be formulated as

$$\begin{aligned} G &= K \cdot A \\ G &= U \Sigma V^{\mathrm{T}} A \\ \underbrace{U^{-1} G}_{G'} &= \Sigma \underbrace{V^{\mathrm{T}} A}_{A'} \\ &\Rightarrow A' = \Sigma^{-1} G' \,, \end{aligned}$$

where we applied the single value decomposition. The matrix Σ is a diagonal matrix containing the singular values. Because of the inversion of Σ, the small singular values are amplifying the error of G. Therefore, a regularization scheme is needed, which will be the maximum entropy method described in this section. The derivation in this section is mainly based on [22], which also gives a detailed analysis of the maximum entropy method.

2.6.1. Maximum Entropy Method

The analytic continuation problem in Matsubara frequencies is solving the inverse of Equation (2.34). In imaginary time we can formulated it with the kernel $K_{\omega\tau}$ as

$$G_\tau = \int_{-\infty}^{\infty} d\omega A_\omega K_{\omega\tau}. \tag{2.81}$$

The inversions of Equations (2.34) and (2.81) are not unique and ill-conditioned and therefore, we have to find the one solution which is the most "likely" one of all. To do so, we need to define a function which tells us how well our fit $\bar{G}_\tau$ agrees with the original imaginary time Green's function G_τ. First we define the covariance matrix

$$C_{\tau\tau'} := \frac{1}{M(M-1)} \sum_j^M \left(G_\tau - G_\tau^{(j)}\right)\left(G_{\tau'} - G_{\tau'}^{(j)}\right), \tag{2.82}$$

where G_τ denotes the expectation value of the Green's function on imaginary time slice τ and $G_\tau^{(j)}$ is the jth sample of a set of M estimates. Thus, Equation (2.82) is an averaged covariance matrix and tells us how errors for different time slices are correlated. Of course the same definition holds in Matsubara space, where one would obtain the matrix $C_{\nu_n\nu'_n}$. Next, we can use the covariance matrix to define a goodness of the fit through

$$\chi^2 := \sum_{\tau,\tau'}^{L} (\bar{G}_\tau - G_\tau)^* C^{-1}_{\tau\tau'} \, (\bar{G}_{\tau'} - G_{\tau'}). \tag{2.83}$$

This requires a back-continuation which is the reverse transformation from a candidate A_ω to a Green's function $\bar{G}_\tau$ on the imaginary axis, using **??**. If the input data are uncorrelated, the matrix $C_{\tau\tau'}$ becomes diagonal, the equation reduces to

$$\chi^2 = \sum_\tau \frac{\left(\bar{G}_\tau - G_\tau\right)^2}{\sigma_\tau^2}, \tag{2.84}$$

where σ_τ is the standard derivation. Since only the back-transformation is well-defined but not the inversion of Equation (2.81), a straight-forward least squares

fitting routine to minimize χ^2 would fail. However, we can add additional conditions, which should regularize the problem and minimize a different function. If an entropy term is added, we obtain the maximum entropy method. The starting point for it is the Bayes' rule from statistics

$$P(A|G) = \frac{P(G|A)P(A)}{P(G)}. \tag{2.85}$$

The "posterior probability" $P(A|G)$ is, given the Green's function G, the probability to obtain the spectral function A. The "likelihood" $P(G|A)$, is the probability when A is given, we get G. $P(G)$ can be ignored, because it is a constant function and not important for the minimization process and drops out. The most tricky probability to obtain is $P(A)$, also known as "prior probability" for A. This part will involve an entropy term, giving the method its name. The basic assumption for the probabilities is that they follow the central limit theorem and therefore we are able to write

$$P(G|A) = P(G|\bar{G}) \propto e^{-\frac{1}{2}\chi^2} = P(G|K * A) \tag{2.86}$$

with $\bar{G}$ in Equation (2.83) replaced by the back transformation $K * A$. For the $P(A)$ calculation we have to use information which known in before, the prior probability. Here, we can force the spectrum to be positive and to have a certain norm. One expression satisfying this is

$$P(A) \propto \exp(\alpha S) \tag{2.87}$$

with

$$S = -\frac{1}{2\pi} \int d\omega \left(A_\omega - D_\omega - A_\omega \ln \left(\frac{A_\omega}{D_\omega} \right) \right). \tag{2.88}$$

The α parameter is a Lagrangian multiplier and S the entropy. The calculation of the entropy involves a function D_ω, also known as default model. In general, the result depends not much on the choice of the default model and a linear default model is often sufficient enough. In interesting aspect, as pointed out in the numerical recipes[40], is that there is nothing universal about the form of the entropy S. Actually, the maximum entropy method can be seen as a more

nonlinear generalized regularization scheme. If we now want to maximize for a given A_ω the probability in Equation (2.85), we have to maximize the exponential e^Q of Equation (2.87), where

$$Q = \alpha S - \frac{1}{2}\chi^2 \,. \tag{2.89}$$

Therefore, one has to find the maximum with respect to A by solving

$$\left.\frac{\delta Q}{\delta A}\right|_{A=A_{\text{opt}}} = 0. \tag{2.90}$$

The result depends implicitly on α through $A(\alpha)$, but α will be fixed and the functional derivative above is evaluated on $A(\alpha_{\text{opt}}) = A_{\text{opt}}$. The methods for fixing the Lagrangian multiplier α are explained in the next paragraph.

2.6.1.1 α - determination

To maximize Equation (2.89) we have to determine the α parameter. For this we can start with the Bayesian inference in Equation (2.85) again, but we rewrite this equation to explicitly depend on α through

$$\begin{aligned} P(A,\alpha|G) &= \frac{P(G|A,\alpha)P(A,\alpha)}{P(G)} = \frac{P(G|A,\alpha)P(A|\alpha)P(\alpha)}{P(G)} \\ &= \frac{P(G|A)P(A|\alpha)P(\alpha)}{P(G)}. \end{aligned} \tag{2.91}$$

By again using the central limit theorem and the definition for the prior probability in Equation (2.87), one obtains the relation

$$P(A,\alpha|G) \propto \frac{P(\alpha)}{Z(\alpha,S)} e^Q, \tag{2.92}$$

with $Z(\alpha,S)$ a normalization factor. The only unknown function is $P(\alpha)$ where one can make a guess. A common choice is the Jeffrey's prior $P(\alpha) \propto 1/\alpha$. If we integrate out the A dependency by integrating over all possible spectra, one gets the probability

$$P(\alpha|G) = \frac{P(A)}{Z(\alpha,S)} \int \mathcal{D}A e^Q \tag{2.93}$$

which is usually a sharply peaked function at some $\alpha = \alpha_{\text{opt}}$. The solution is then the spectrum A, using $\alpha = \alpha_{\text{opt}}$ and maximizing Q. Though, A depends on α and α on A and therefore, an iterative scheme has to be applied to obtain the final solution. This whole procedure is know as the classical maximum entropy method and was used for computing the dynamical quantities in this project. However, there are more ways to determine the α value and another well-known method is the Bryan's method. Bryan's method calculates for each α (usually a discretized α grid) the A_α, maximizing Q. The final solution is the calculated through the integration

$$A_\omega = \int d\alpha A_{\alpha\omega} P(\alpha|G) \tag{2.94}$$

and can be seen as a weighted average of all possible A_α. Usually, this method is more computationally intensive and therefore slower.

2.6.1.2 Correlated Error

In the previous Equation (2.82), we introduced the correlation matrix $C_{\tau\tau'}$ which is also known as the covariance matrix. This matrix tells us, how the data at an imaginary time point τ is correlated with another imaginary time point τ'. The diagonal is the variance and all the off-diagonal elements are the covariances. In the case where the covariance matrix entries are zero or very small, the data are uncorrelated and basically completely random distributed. In terms of linear algebra we can also say, that the covariance matrix is in its own eigen basis and therefore diagonal. This also means, that the data vector and kernel are in the eigen bases of the covariance matrix and thus, we can simply apply the Equation (2.84) for calculating χ^2. But what if we have data which are correlated over τ? To still be able to use the previous equations of the maximum entropy method we have to rotate the kernel K and the data vector G in a basis where the covariance matrix is diagonal. Obviously, this is the basis spanned by the eigen vectors of the covariance matrix. Therefore, we have to diagonalize C and rotate the kernel

matrix and data vector through a matrix vector multiplication. Thus,

$$C' = U^{-1}CU \tag{2.95a}$$
$$K' = U^{-1}K \tag{2.95b}$$
$$G' = U^{-1}G\,, \tag{2.95c}$$

where U is the matrix of the eigenvectors. The new errors can then be calculate through taking the square root of the eigen values λ_i of the covariance matrix, thus

$$\sigma_i' = \sqrt{\lambda_i} \tag{2.96}$$

Using the covariance matrix actually improved our results. Especially in DQMC, it made it possible to compute dynamic correlation function for U and β values where the quality of data is lower, due to sign problem. We also found, that the assumption of uncorrelated error in DQMC is in general not given.

Chapter 3

Results

In this chapter we will discuss the results for the Hubbard model on the Kagome lattice and compare the two methods DQMC and DMFT described in the previous Sections 2.4 and 2.5. DQMC is very limited in the size of the system and strongly depending on the geometry of the lattice. In the case of a Kagome structure it is limiting us in temperature and interaction U due to the sign problem, where the sign problem in DMFT is absent. However, the sign problem for DQMC starts at a temperature where correlation effects are already important, and therefore we are able to investigate electronic correlation effects. Figures 3.1 and 3.2 show the plots of the sign for different temperatures and interacting strengths for DQMC. The geometric dependence of the sign problem in DQMC was investigated in detail by Iglovikov et. al.[20]. Our results for the sign at $\beta = 4$, $U = 6$ and $n = 1$, as shown in Figures 3.1 and 3.2, are in good agreement with Figure 14 in their paper[20].

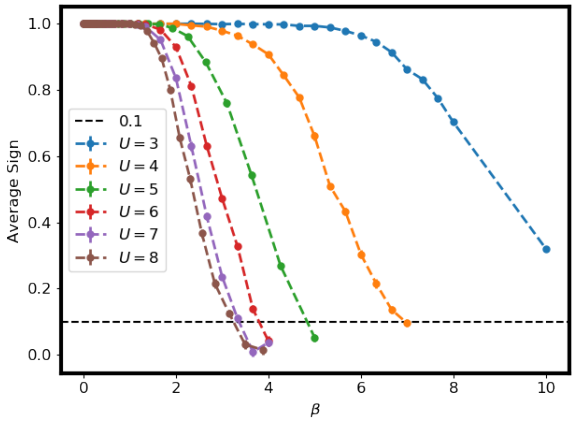

Figure 3.1: Average sign in DQMC for different U values and different temperatures at $n = 1$.

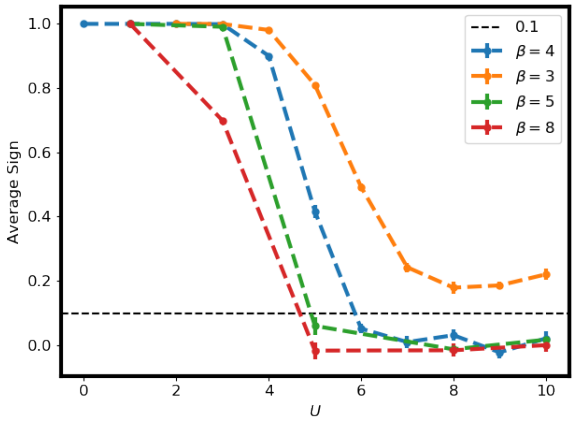

Figure 3.2: Average sign in DQMC for different temperatures β and interactions U at half filling ($n = 1$).

We can see: if we want to have a U-range from 1 to 10 and want to keep the sign above the value 0.1, only the temperature $\beta = 3$ satisfies this. Therefore, we chose in the following $\beta = 3$, in order to investigate the Mott metal-insulator transition and are able to compare it with DMFT. For the weaker correlation $U = 3$, we are able to do calculations down to temperatures $\beta = 10$. In addition we will also present results along a k-path.

Most of the results involve the post-processing step of analytic continuation and,

as we mentioned in Section 2.6, this is an ill-conditioned problem and the solution is not unique. Therefore, after obtaining a result analytic continued to the real axis, it is not clear whether the best or most physical solution is found. One big problem is to distinguish between physical peaks and artifacts of the maximum entropy method. To improve the outcome, one can do a couple of checks. One check is to refine the frequency grid for the computation. The frequency grid should be such that major features of the non-interacting spectra are resolved. By looking at the non-interacting density of states, we can identify the features of the spectral function for the limits of zero temperature and $U \to 0$ (see Section 2.3). With increasing U, above a certain U-value, a gap around the Fermi energy opens and the system undergoes the phase transition to an insulator. In this case, one can estimate the position of the Hubbard bands with $\pm U/2$. For $U >> 1$ the spectrum should feature the non-interacting density of states twice, separated with the Mott gap. With these information we can refine the frequency grid, to better resolve the occurring peaks. A second check is to vary the error. On the one hand, when the error is too small, one is over-fitting the spectrum and sharp peaks are appearing. On the other hand, when the error is too big, the spectrum will look similar to the default model. If the spectrum stays stable when varying the error in small steps, it indicates that the physical spectrum is found. In order to chose a maximum entropy program, we tried out three different implementations and applied error rescaling and used different frequency grids. The first program we used is from Levy et. al.[29], the second one is from Bergeron[4] and the third one is a from Kaufmann[25]. Let us briefly mention the main features and differences of the three programs:

1. **Levy et. al** offers various kernels for bosonic and fermionic data in Matsubara, imaginary time or Legendre representation with or without particle hole symmetry. You can choose from various pre-defined frequency grids and default models.

2. **Bergeron** implemented features for detecting peaks and automatically refine the grid in regions around peaks. It is very sophisticated in terms of providing parameters for every step during the analytic continuation and for optimizing results. However, the biggest difference between the other two programs is, that it does not use the classical nor Bryan's method to determine the

optimal α. Instead it locates the optimal α by finding the regions where only noise and only information is fitted and uses the crossover of these regions. Another difference is that imaginary time data are first Fourier transformed into Matsubara frequencies and then cubic spline interpolated. This allows one to compute the Green's function piecewise with high numerical accuracy.

3. **Kaufmann**'s Python package is a library containing the necessary routines for analytical continuation, but the users are encouraged to write their own scripts. Thus, the users have to choose the alpha determination, kernel, frequency grid and default models by themselfs. This provides a lot of freedom and flexibility for optimization. For determining the optimal α you can choose between the classical or Bryan's method.

Because of its flexibility and customization possibilities, we chose the maximum entropy program by Kaufmann. Because the program is mainly written in Python, it makes it easier to read in the raw data from a hdf5 file and process them directly in Python instead of generating input files first. Therefore, we were able to do analytic continuation for thousands of points at once, which was necessary to generate k-resolved correlations on the real axis. Another advantage is that we could extend the code to support covariance matrices described at the end of Section 2.6.1. This turned out to be a major improvement for the DQMC results. In order to calculate the covariance e.g. for Green's functions, we need a data set containing all Green's functions from many independent simulations. The DMFT program w2dynamics[53] is supporting this by writing out the Green's functions of each statistic run into an hdf5 file. From that, one can do the necessary post-processing steps, e.g. bootstrap or jackknife resampling, to obtain the averaged result and the covariance matrix. The DQMC program QUEST (http://quest.ucdavis.edu), does not support this out of the box. The program was designed to calculate statistics internally and only writes out the averaged results, which avoids generating huge output files. However, if we want to calculate the covariance matrix we need the result of every statistic run. Therefore, we built a MPI (Message Passing Interface) Python script which is able to run DQMC simulations on multiple nodes and with different random seeds. The different random seeds ensure, that the sequence of Monte Carlo moves are independent from each other and so are the simulations. In this way, we obtain for each temperature β and Hubbard U, that we are in-

terested in, 320 simulations. Each of these simulations used 500 imaginary time slices, 600 warmup sweeps and 3000 measurement sweeps. We want to note here, that the amount of 500 imaginary time slices in DQMC is very unusual, because $\Delta\tau$ becomes unnecessary small (for $\beta = 3$). However, to obtain decent resolve dynamical quantities, one needs to have a dens imaginary time grid. The lattice size are 5×5 unit cells and therefore 75 sites with periodic boundary conditions. One simulation with these parameters took around two days on a Intel Xenon IvyBridge-EP E5-2650v2 CPU core. For some results, we analyzed the correlations between the statistic runs and we found a highly non-diagonal covariance matrix, where the matrix off-diagonal elements are of the same magnitude as the diagonal ones. Figure 3.3 shows a heat plot of the covariance matrix of the Green's functions for $U = 3$ and $\beta = 3$.

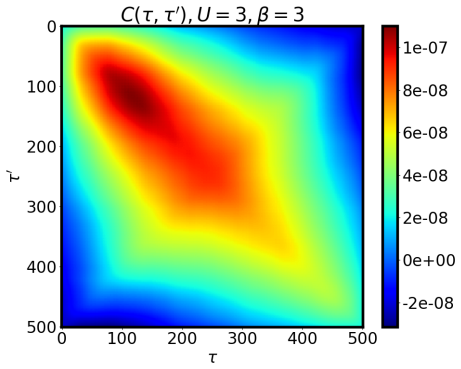

Figure 3.3: Covariance matrix of the local imaginary time Green's function G_τ for $U = 3$ and $\beta = 3$ with 320 DQMC statistic runs. It can clearly be seen that the matrix is not diagonal and therefore, the simulations are correlated along the τ-axis.

Because of this strong correlation in τ, it is crucial to include the covariance in maximum entropy and apply the method described at the end of Section 2.6.1.

3.1. Half Filling

In this section we present the results for a half filled Kagome lattice. As we mentioned in Section 2.3, the spectrum of the Kagome lattice is not particle-hole symmetric, and therefore we need to find the chemical potential which yields half filling. Numerically, this is done iteratively and the DMFT program w2dyamics

provides such an iterative determining of the chemical potential. However, the DQMC program QUEST does not support an automatic determining of the chemical potential. Therefore, we implemented the method described in Section 2.4.6. We created a new Fortran module in the QUEST program, built a Python wrapper around it and implemented the "false position method" in a Python script, which calls the underlying Fortran routines of QUEST. The package, including the Fortran module and Python script is available on github[50]. The top plot of Figure 3.4 shows the resulting chemical potentials for different inverse temperatures and different Hubbard interactions U. The bottom plot shows the corresponding densities obtained, when running a full simulation using the calculated chemical potentials. Because of the sign problem, we neglected data points where the sign is below than 0.1. It is important to mention that for $U \approx 8$ the Mott gap in DQMC spectra is already present and therefore, for $U > 8$ the chemical potential is not well defined any more. The Fermi level will then lay within the gap and thus, the results for μ become arbitrary within the gap.

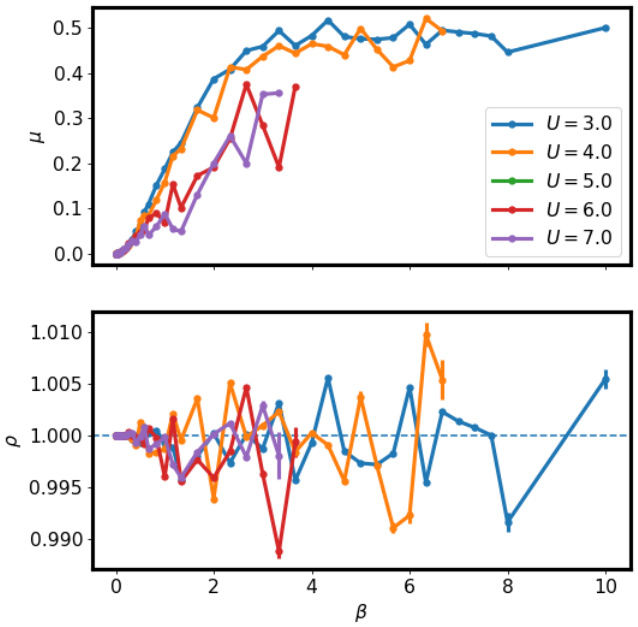

Figure 3.4: The calculated DQMC chemical potentials μ for different U values vs. densities n at temperatures where the average sign is $>= 0.1$.

3.1.1. Mott-Hubbard Metal-Insulator Transition

In Section 2.6 we described the maximum entropy method, which we used to obtain the Green's function in real frequencies. The imaginary part of the real frequency Green's function is directly related to the interacting particle spectrum (see Equation (2.38)) and can be compared with experimental measurements such as photo emission spectroscopy (PES) and angle resolved photo emission spectroscopy (ARPES). Thus, the spectral function can tell us much about the interacting system. Let us start to compare the DMFT and DQMC integrated spectral functions A_ω. For this, we analytic continued the local Green's function. Figures 3.7 and 3.8 shows obtained spectra after applying the maximum entropy method. Up to $U = 5$ the spectra look similar. However, one can clearly see the differences starting with $U > 5$. In particular there is a Mott Hubbard metal-insulator transition in DQMC starting between $U = 6$ and $U = 7$, and the gap forming between $U = 8$ and $U = 9$. In DMFT the Mott Hubbard metal-insulator transition is starting later between $U = 8$ and $U = 9$. At $U = 10$ the gap as almost formed and therefore we assume, that maximum entropy would show an open gap between $U = 10$ and $U = 11$.

In DQMC we can use the spatial dependence of the Green's function to do a Fourier transformation into k-space and then to do an analytic continuation for obtaining a momentum resolved spectrum. The only downside is, that we only have a few r-points because of the small grid size DQMC is using. In particular, with lattice size of 5×5 unit cells, we would only have 25 k points. However, we can use a much denser k-grid for Fourier transformation, as long the Green's function is decaying fast enough around the center $r = 0$. This is an approximation, where we truncate the Fourier series and neglect components higher than a certain order. Figure 3.5 shows the value of the Green's function for different distances r. As it can be seen, only the Green's function components of the first few smallest $\boldsymbol{r}$ are playing a role in the Fourier transformation. Therefore, our assumption is satisfied and we defined a cutoff distance R_{cutoff} and neglected all contributions above R_{cutoff}. One can write then the Fourier transformation of the Green's function as

$$G_{\boldsymbol{k}\tau} = \sum_{|\boldsymbol{r}|<R_{\text{cutoff}}} G_{\boldsymbol{r}\tau}\, e^{i\boldsymbol{k}\boldsymbol{r}}\,, \tag{3.1}$$

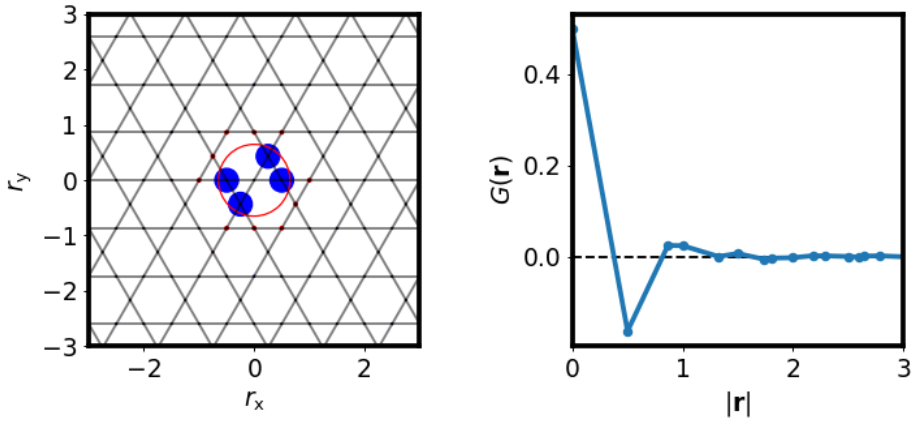

Figure 3.5: The value of the DQMC equal-time Green's function for $U = 5$ and $\beta = 3$ for different distances. On the left are the values drawn onto the Kagome lattice, where the radii are direct proportional to the values. The red hollow circle denotes the local Green's function at $r = 0$, the full circles are the non-local ones. Red color means positive value and blue negative value. On the right is the corresponding one-dimensional plot.

The cutoff distance R_{cutoff} was chosen as the distance for which the value to error ratio of the Green's function exceeds a certain limit. That is, the distance where the data points became unreliable. By using Equation (3.1) we calculated the interacting band structure along the first Brillouin zone (BZ) path $\Gamma - M' - K' - \Gamma$. However, to include all information, we need to include points from the extended BZ (EBZ), because not all information is contained within the first BZ. Thus, in order to calculate the path, we have to map all possible first BZ path segments of the EBZ back, onto the corresponding first BZ path segments (in this way we obtain three bonds for the first BZ instead of one bond for the EBZ). Figure 3.6 shows all possible segments of the $\Gamma - M' - K' - \Gamma$ path in the EBZ, denoted with colors blue, red and green.

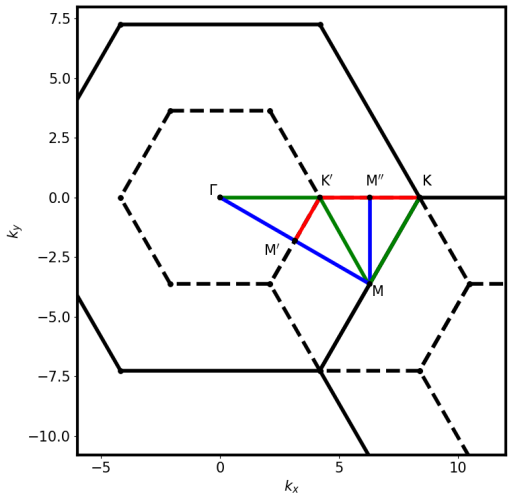

Figure 3.6: All possible first BZ (dashed area around Γ) path segments of $\Gamma - M' - K' - \Gamma$ in EBZ (solid area). The green are all $\Gamma - K'$ segments, which are $\Gamma - K'$, $M - K$ and $M - K'$ respectively. The red are all $K' - M'$ segments, which are $K' - M'$, $M'' - K'$ and $M'' - K$ respectively. The blue ones are all the $M' - \Gamma$ segments, which are $M' - \Gamma$, $M - M'$ and $M - M''$ respectively.

Figure 3.9 shows the obtained band structures. Except for the spectrum at $U = 3$ and $\beta = 3$, where we rescaled the error with a factor of 200, we did not apply any error rescaling and only used the covariance matrix as input for the error. This worked surprisingly well for generating smooth band structures. For $U = 3$ to $U = 6$, the bands follow the non-interacting bands and with increasing U only a broadening can be seen. While the broadening at $U = 3$ is certainly due to a mixture of physical self-energy effects and artifacts of the maximum entropy, the increasing broadening from $U = 3$ to $U = 6$ can be identified with a physical effect: strong correlations lead to reduced life times, i.e, a larger broadening. Starting with $U = 7$ the band structure starts breaking up into two parts, in agreement with Figure 3.8. With increasing interaction strength, the flat band is shifting up and merges with the appearing Hubbard band on the top. Starting with $U = 8$, the gap is forming and is fully developed at $U = 10$ with a width around 3, also in agreement with Figure 3.8.

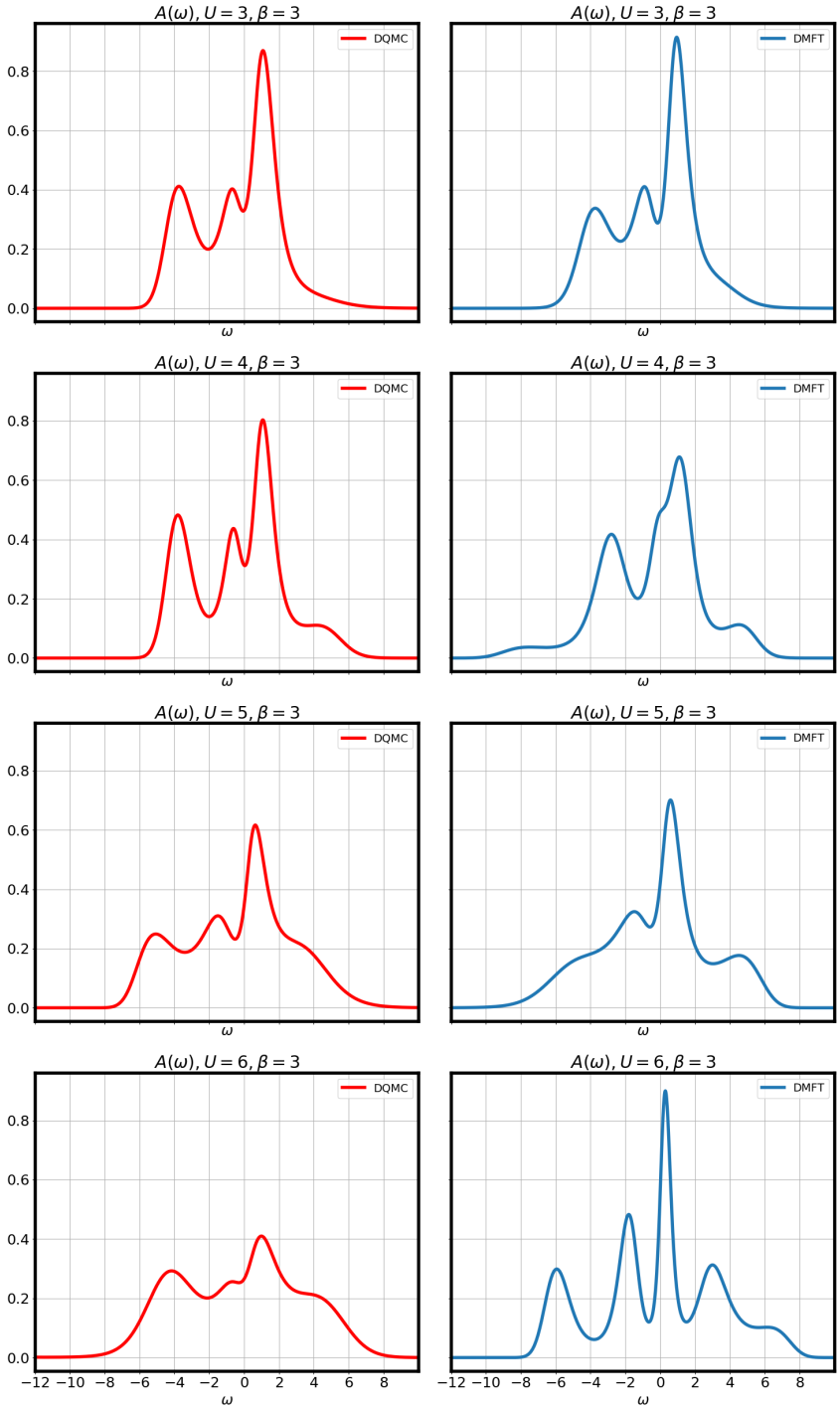

Figure 3.7: k-integrated spectral functions A_ω at $\beta = 3$ and $U = 3, 4, 5$ and 6. The left column are the DQMC results and the right column the DMFT results.

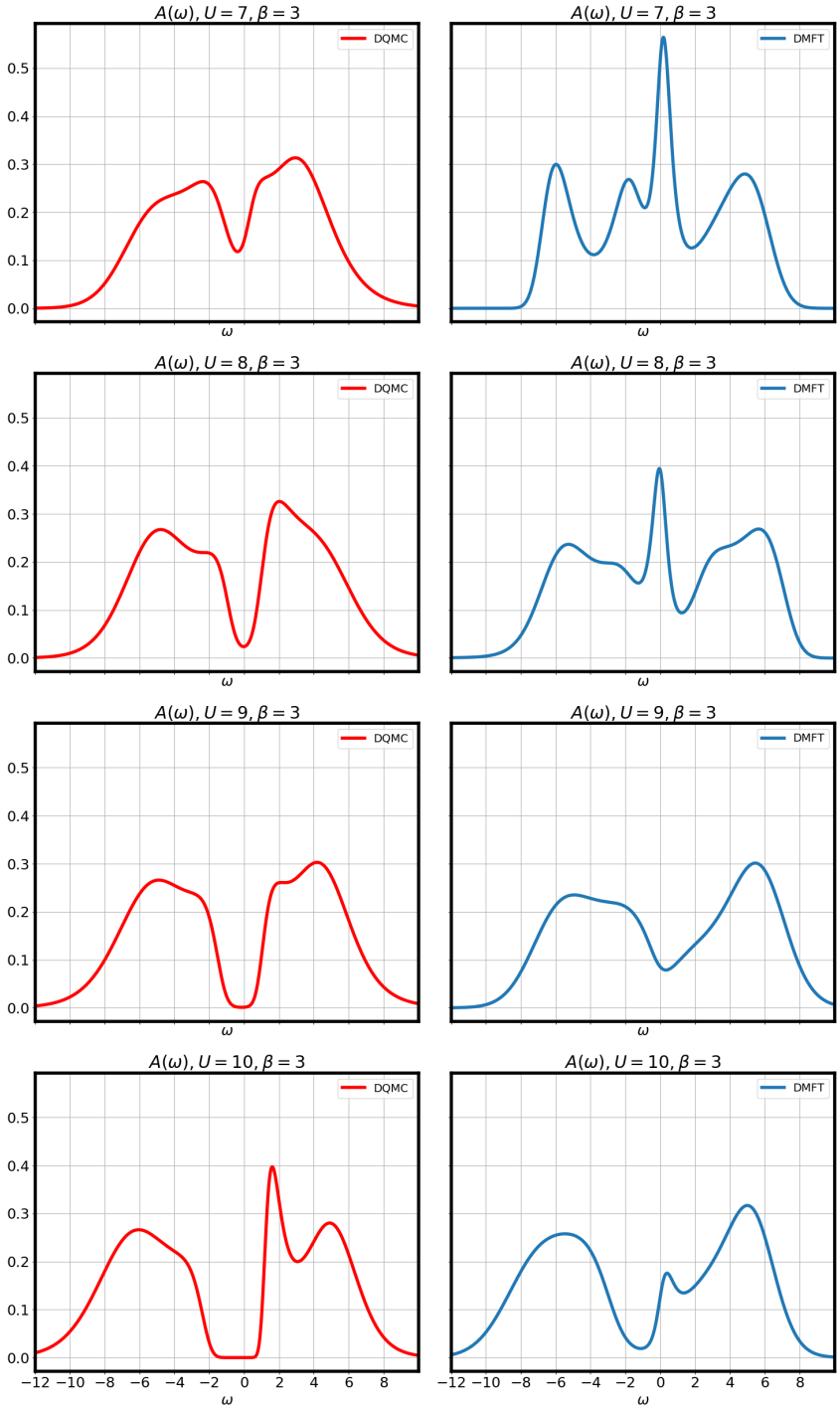

Figure 3.8: k-integrated spectral functions A_ω at $\beta = 3$ and $U = 7, 8, 9$ and 10. The left column are the DQMC results and the right column the DMFT results.

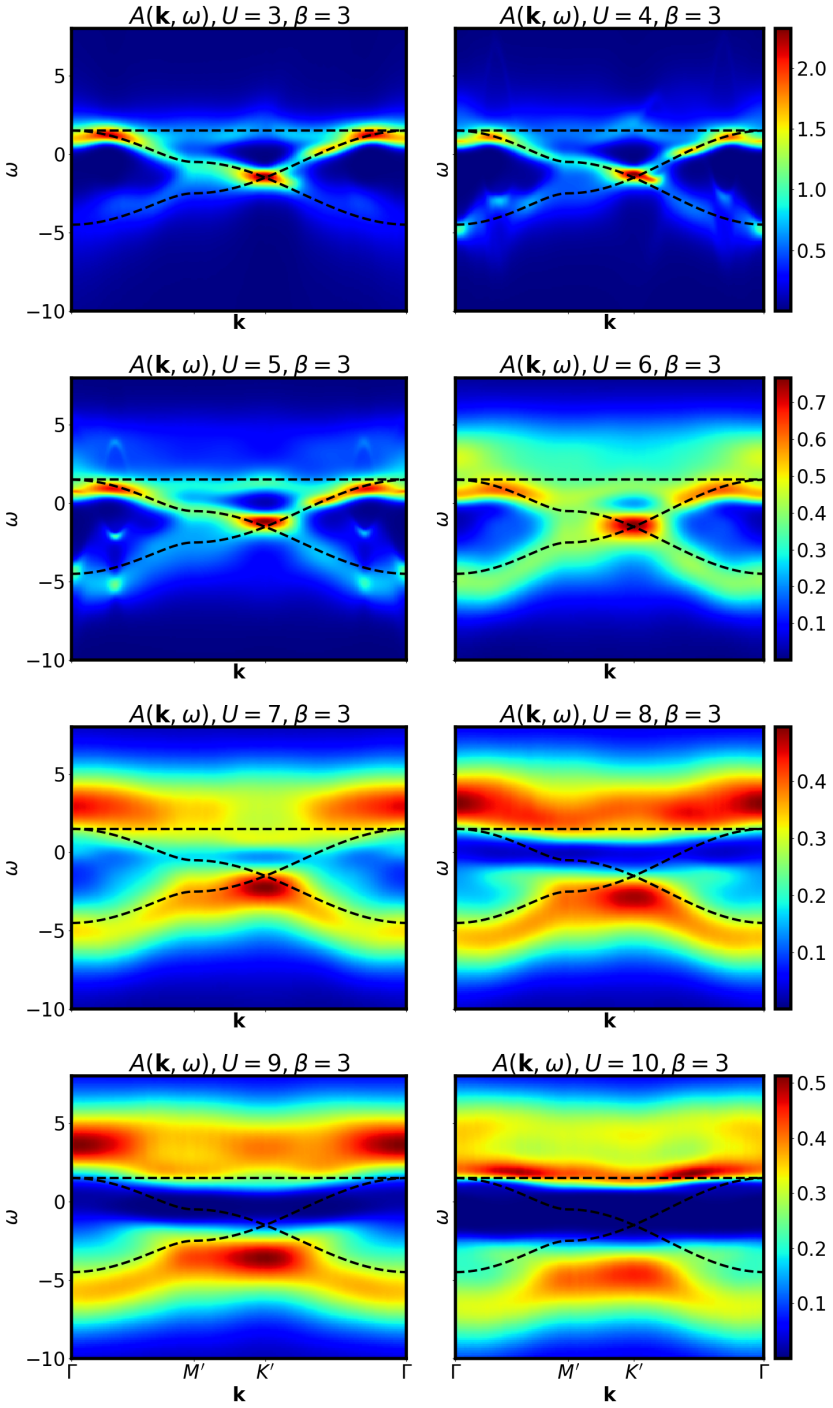

Figure 3.9: DQMC k-resolved spectral functions $A_{\boldsymbol{k},\omega}$ at $\beta = 3$ and $U = 3, 4, \ldots, 10$ along the high symmetry path $\Gamma - M' - K' - \Gamma$ of the first BZ. The black dashed line is the band structure of the non-interacting system in tight-binding approximation, shifted by the chemical potential $\mu = 0.502$ for half filling.

3.1.2. Temperature Dependence at Weak Interaction

In this section we discuss the electronic correlations for the weak interaction $U = 3$. Looking back at Figure 3.1, we see that for $U = 3$, we are able in DQMC to do calculation down to $\beta = 10$. Figure 3.10 shows the integrated spectral functions for $\beta = 6, 8$ and 10.

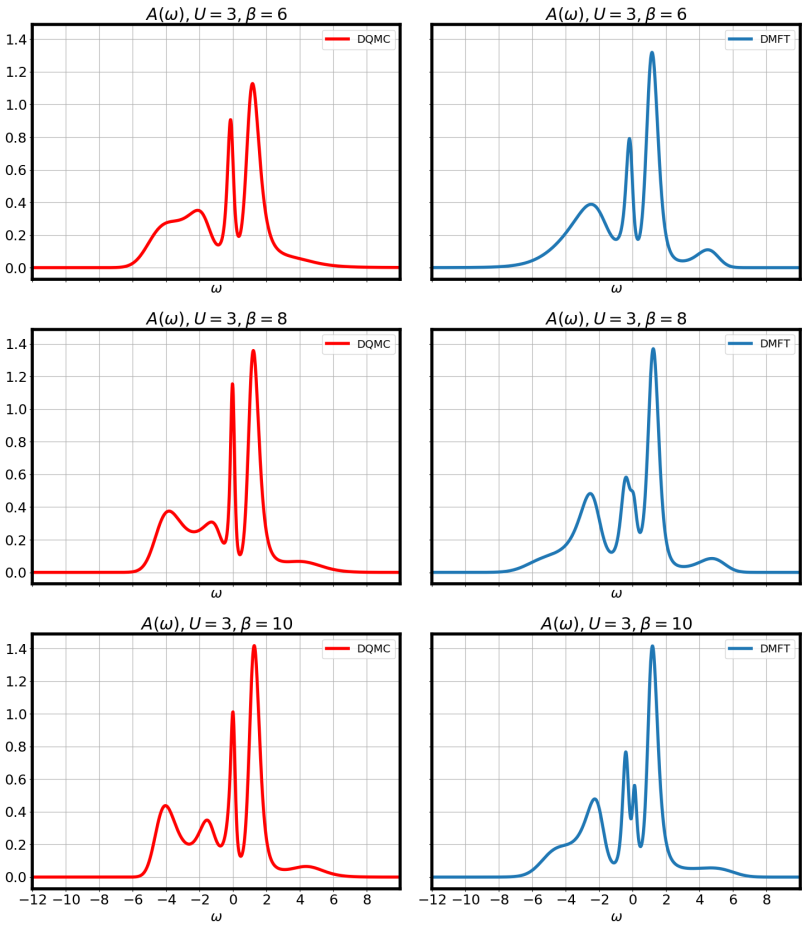

Figure 3.10: Integrated spectral functions A_ω at $\beta = 6, 8, 10$ and $U = 3$. The left column are the DQMC results and the right column the DMFT results.

The main difference between the above DMFT and DQMC spectra is in the region -6 to 0. DQMC features in this region three peaks close to -4, -2 and 0, which are getting more pronounced with lower temperature. However, DMFT only has two peaks close to -3 and 0, where the latter one splits up when temperature is

lowered.

3.1.3. Magnetic Structure Factor

In this section we discuss the calculated magnetic properties of the Kagome lattice, in particular the magnetic structure factor. The magnetic structure factor is directly related to neutron scattering experiments[16]. The equal-time magnetic structure factor is defined as the Fourier transformation of the real space spin-spin correlation. Thus,

$$S_{\boldsymbol{q}} = \sum_{\boldsymbol{r}_i,\boldsymbol{r}_j} \left\langle S^{\mathrm{z}}_{\boldsymbol{r}_i} S^{\mathrm{z}}_{\boldsymbol{r}_j} \right\rangle e^{i\boldsymbol{q}(\boldsymbol{r}_i-\boldsymbol{r}_j)} \,. \tag{3.2}$$

For a energy resolved spectrum, one can define the dynamic magnetic structure factor as

$$S_{\boldsymbol{q},\tau} = \sum_{\boldsymbol{r}_i,\boldsymbol{r}_j} \left\langle S^{\mathrm{z}}_{\boldsymbol{r}_i,\tau} S^{\mathrm{z}}_{\boldsymbol{r}_j,0} \right\rangle e^{i\boldsymbol{q}(\boldsymbol{r}_i-\boldsymbol{r}_j)} \tag{3.3}$$

and

$$S_{\boldsymbol{q},\omega} = -\frac{1}{\pi}\Im\left[\frac{\chi_{\boldsymbol{q},\omega}}{1-e^{-\beta\omega}}\right] = -\frac{1}{\pi}\Im\left[\frac{\omega B_{\boldsymbol{q},\omega}}{1-e^{-\beta\omega}}\right] \,, \tag{3.4}$$

where the operator $\Im$ is returning the imaginary part, $B_{\boldsymbol{q},\omega}$ is defined in Equation (2.40) and $\chi_{\boldsymbol{q},\omega}$ is the magnetic susceptibility. Let us from here on drop the word "magnetic" from all future structure factor names. All results below, are generated with DQMC. Calculating the equal-time structure factor in Equation (3.2) only requires a Fourier transformation, where one can use the fact again, that the spin-spin correlations are decaying fast with increasing distance. Hence, we applied the same method as for the k-resolved spectra in Section 3.1.1. Figure 3.11 compares the obtained equal-time structure factors for $U = 3, 4, \ldots, 10$ and $\beta = 3$ and Figure 3.12 compares the the equal-time structure factors for $U = 3$ and $\beta = 3, 6, 8$ and 10. Drawn into the plots are the first BZ in dashed lines and the extended BZ in solid lines with its three symmetry points Γ, M and K.

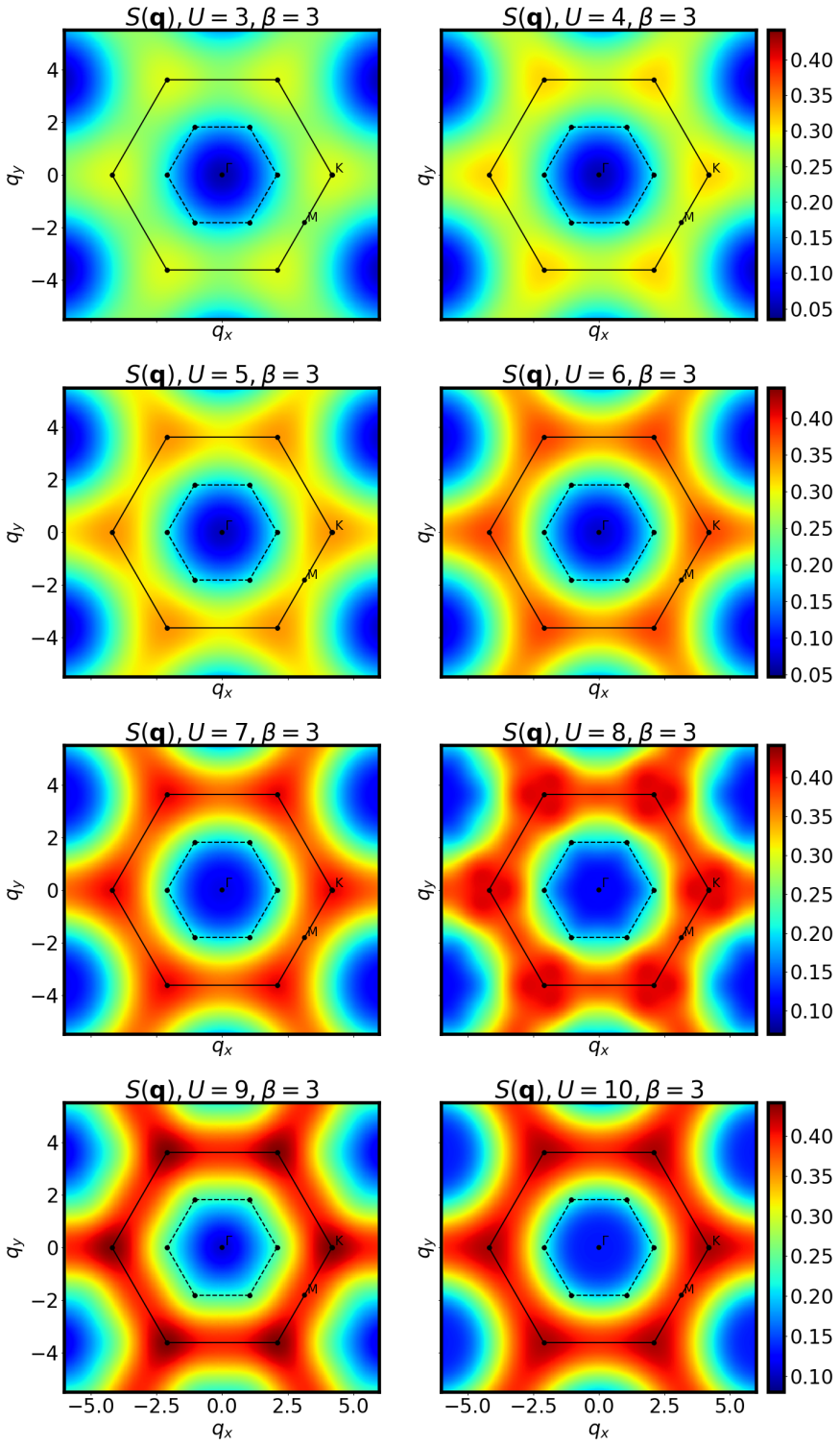

Figure 3.11: DQMC equal-time structure factor $S_{\boldsymbol{q}}$ in the EBZ at $\beta = 3$ and $U = 3, 4, \ldots, 10$.

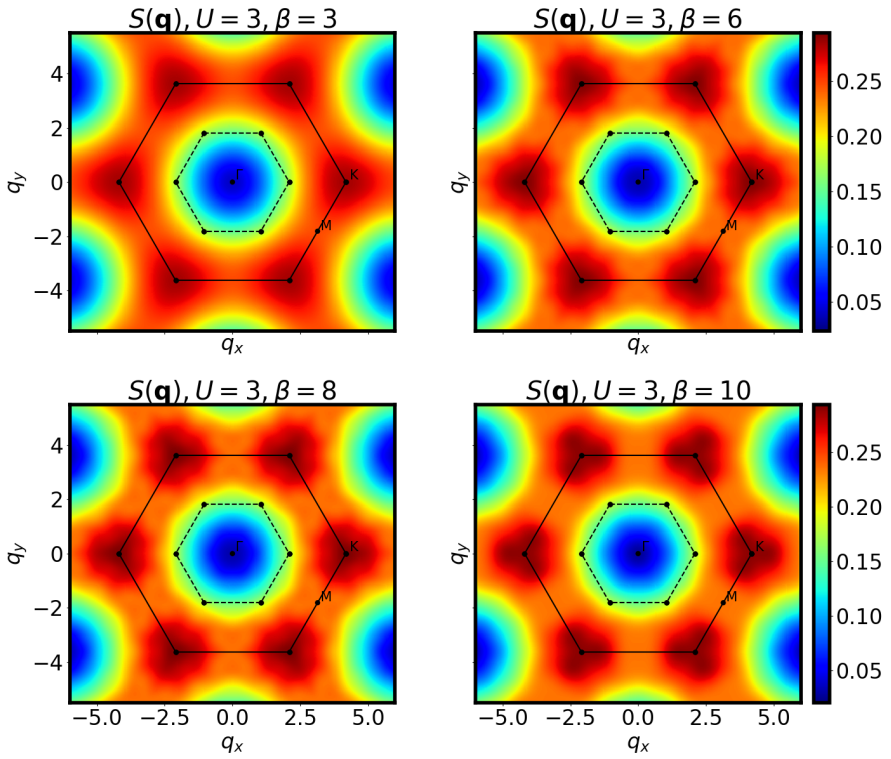

Figure 3.12: DQMC equal-time structure factor $S_{\boldsymbol{q}}$ in the EBZ at $U = 3$ and $\beta = 3, 6, 8, 10$.

A larger structure factor is formed at the M point and K point and in between forming a ring-like structure with the hexagonal symmetry still visible. It can be seen that most of the intensity is almost only in the EBZ, in good agreement with the results in Heisenberg approximation by Sherman[46]. More specifically in the spin liquid, the structure factors are featuring triangles where the corners are close to the M points and the centers are on the K points. With increasing U the corners of the triangles are getting sharper and thinner. Only at $U = 8$ a rounder pattern around K can be seen, which is probably resulting from a lower quality of data. Overall, the shapes of the different structure factors for different U and $\beta = 3$ are very similar. The intensity of $S_{\boldsymbol{q}}$ is increasing with U and has its maximum for $U = 9$ at the K point. For the equal-time structure factors with $U = 3$ at temperatures $\beta = 3, 6, 8, 10$ only the shape is slightly changing but the intensity stays the same.

More information is contained in the dynamic structure factors. To obtain the dynamic structure factors, a Fourier transformation and an analytic continuation is needed to get from $\chi_{\boldsymbol{r},\tau}$ to $\chi_{\boldsymbol{q},\omega}$. The difference, compared to Section 3.1.1 is, that we have to use a bosonic kernel instead a fermionic one for analytic continuation. We calculated the dynamic structure factor along the EBZ path $\Gamma - M - K - \Gamma$. For the analytic continuation we chose an equidistant frequency grid with 500 points between 0 and $20/U$ and an equidistant grid with 200 points from $20/U$ to 20. The plotted region is from 0 to $20/U$, where the region from $20/U$ to 20 is only used to ensure well behaved asymptotic. Here, we scaled the frequency by $1/U$ for keeping the magnetic coupling which is $J = 4t^2/U$ approximately constant. Further, we used the covariance matrix of the data and no error rescaling. Figures 3.13 and 3.14 show the results. With the scaling of $1/U$ the structure factor essentially stays the same from $U = 6$ to $U = 10$, despite the Mott-Hubbard transition.

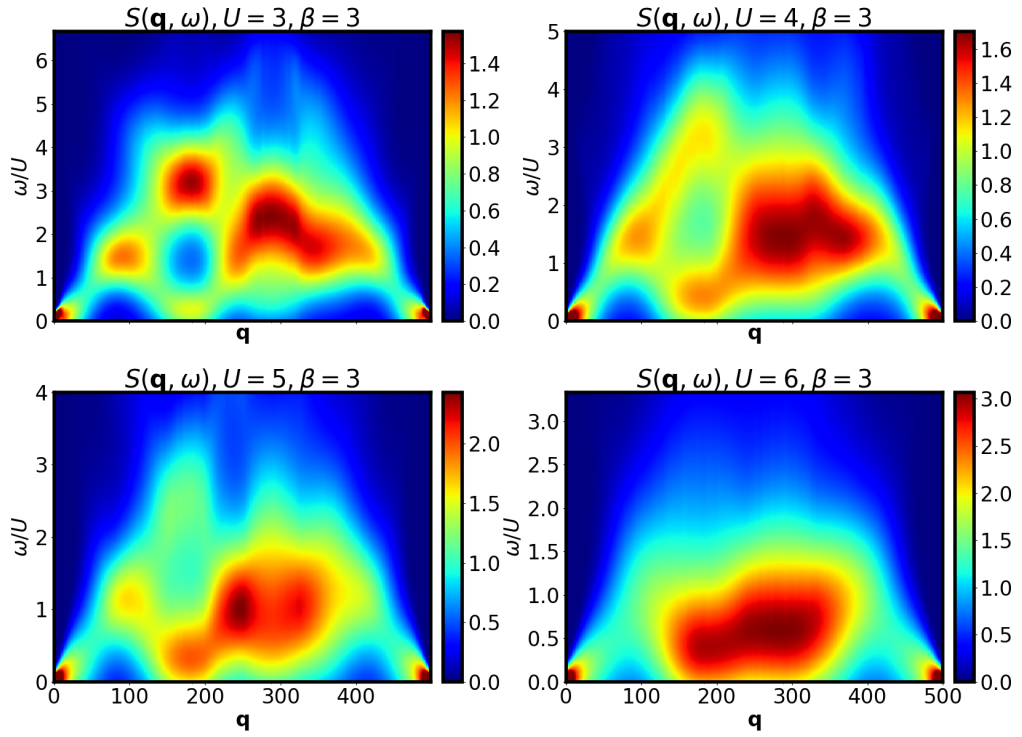

Figure 3.13: DQMC dynamic structure factor $S_{\boldsymbol{q},\omega}$ at $\beta = 3$ and $U = 3, 4, 5$ and 6 along the high symmetry path $\Gamma - M - K - \Gamma$ in the EBZ.

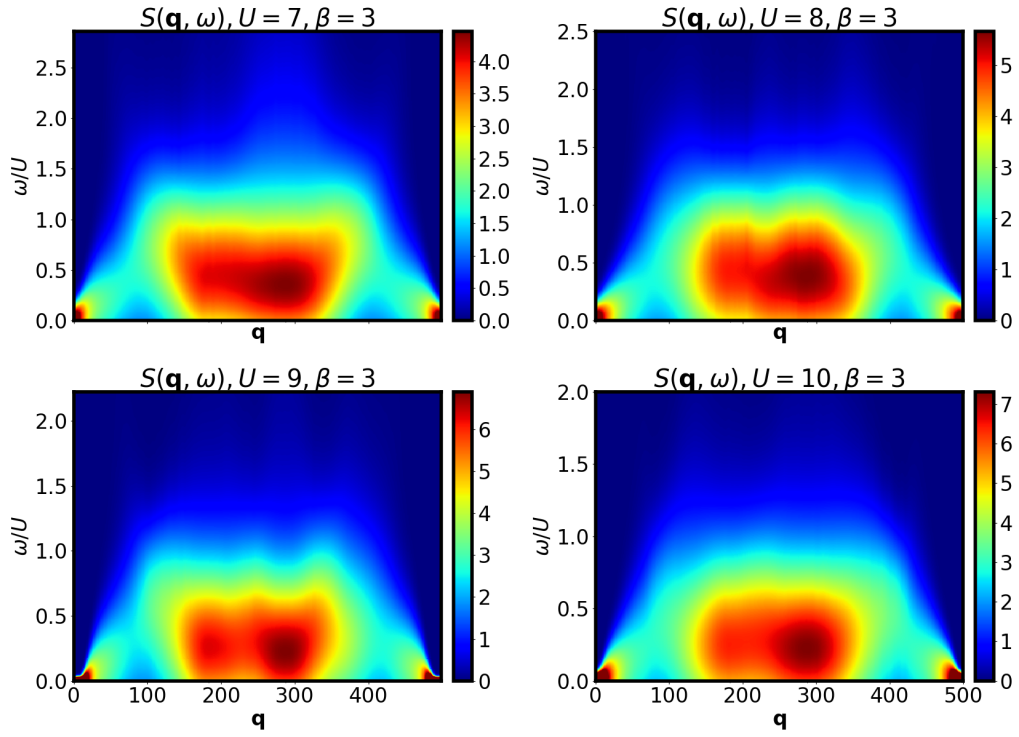

Figure 3.14: DQMC dynamic structure factor $S_{\boldsymbol{q},\omega}$ at $\beta = 3$ and $U = 7, 8, 9$ and 10 along the high symmetry path $\Gamma - M - K - \Gamma$ in the EBZ.

3.2. Half Filled Flat Band

In Section 2.3 we listed the main properties of the Kagome system, where one outstanding feature is the flat band. When using the Hubbard Hamiltonian definition in Equation (2.48) with $t > 0$ and changing the filling to 5/6, one obtains a half filled flat band. The same is true for $t < 0$ with 1/6 filling, related to the former cause by a particle-hole transformation. In this special case, the Kagome lattice may be expected to exhibit flat band ferromagnetism, as it was first rigorously shown by Mielke[34] and reviewed and extended by Tasaki[51]. Therefore the localized electrons in the flat band are developing long-range order. Such calculations are an optimal case for DMFT, where interactions are purely local and k-independent. However, for DQMC it is quite the opposite, where lattice dimensions are usually very small and long-ranging correlation effects are difficult to obtain. Further, it is challenging in DQMC to get a ferromagnetic system as

it does calculations in real space. When having ferromagnetism, the symmetry is broken and in case of Kagome in two possible ways. Therefore, the outcome of the Monte Carlo simulations is arbitrary with respect to the two magnetic orientations possible. This means when running many simulations, on average the net spin should cancels out. Indeed, this is what we found when running DQMC calculations on Kagome with half filled flat band. Figure 3.15 shows the susceptibility $\chi_{\boldsymbol{r}}$ for different distances $|\boldsymbol{r}|$.

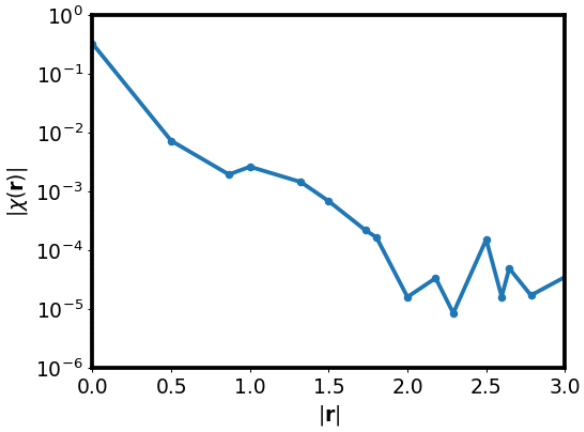

Figure 3.15: DQMC equal-time susceptibility for $U = 3$ and $\beta = 5$ at 5/6 filling. The plot shows the values for different distances. Besides the local susceptibility, all other contributions are basically vanishing.

Unfortunately, because of the above mentioned reasons, we were not able to investigate the ferromagnetism in the half filled flat band of the Kagome lattice with DQMC.

Chapter 4

Conclusion and Outlook

To solve the Hubbard model, we used the fundamentally different methods DQMC and DMFT and investigated the following three cases: First, the Mott-Hubbard metal-insulator transition at half filling through the k-integrated and k-resolved spectral functions, where we compared the DQMC and DMFT results. Second, the magnetic structure factor at half filling with DQMC, at the same temperature and interaction strengths as we used for the Mott-Hubbard metal-insulator transition calculations. Third, the half filled flat-band case with DQMC.

We were able to find the Mott-Hubbard metal-insulator transition in DQMC and DMFT, albeit at different interaction strengths. The equal-time magnetic structure factors are featuring intensity patterns, which are in a good agreement with previous publications. Further, we calculated the dynamic magnetic structure factor, where we could see a flattening of the intensity pattern with increasing electronic interaction. Due to the frustration in the half-filled case, the correlation are short-ranged and the DQMC method turned out to be a good fit. Hence, the restriction to a finite-sized lattice is well justified. For the case of flat band doping, ferromagnetism is anticipated, i.e. the spatial correlation length is expected to be large. However, we were unable to find it in DQMC. In order to obtain the spectral functions and magnetic structure factors, tools for various post-processing steps were developed. Most of them are footing on the analytic continuation of imaginary-time Green's function with the maximum entropy method. We found out that the common assumption of uncorrelated data in DQMC is generally not

fulfilled and it is crucial to take this into consideration.

The DQMC and DMFT methods are used since decades and still constantly improved. In DMFT, a central object is the local self-energy, and with diagrammatic extensions it is possible to even obtain non-local contributions to it. In DQMC, non-local correlations are included naturally within the algorithm. However, the self-energy is usually not calculated. For a future work, it would be very interesting to implement a self-energy measurement in DQMC, in the spirit of Refs[14, 15]. This would allow for comparison with non-local self-energies from diagrammatic methods e.g. DΓA.

Bibliography

[1] N.W. Ashcroft and N.D. Mermin. *Solid State Physics*. Cengage Learning, 2011. ISBN: 9788131500521. URL: https://books.google.at/books?id=x_s_YAAACAAJ.

[2] Alexandre Zagoskin (auth.) *Quantum Theory of Many-Body Systems: Techniques and Applications*. 2nd ed. Graduate Texts in Physics. Springer International Publishing, 2014. ISBN: 978-3-319-07048-3,978-3-319-07049-0.

[3] Balents Leon. "Spin liquids in frustrated magnets". In: *Nature* 464.7286 (2010). 10.1038/nature08917, pp. 199–208. ISSN: 0028-0836. DOI: http://dx.doi.org/10.1038/nature08917.

[4] Dominic Bergeron and A-MS Tremblay. "Algorithms for optimized maximum entropy and diagnostic tools for analytic continuation". In: *Physical Review E* 94.2 (2016), p. 023303.

[5] R. Blankenbecler, D. J. Scalapino, and R. L. Sugar. "Monte Carlo calculations of coupled boson-fermion systems. I". In: *Phys. Rev. D* 24 (8 1981), pp. 2278–2286. DOI: 10.1103/PhysRevD.24.2278. URL: https://link.aps.org/doi/10.1103/PhysRevD.24.2278.

[6] Felix Bloch. "Über die Quantenmechanik der Elektronen in Kristallgittern". In: *Zeitschrift für Physik* 52.7 (1929), pp. 555–600. ISSN: 0044-3328. DOI: 10.1007/BF01339455. URL: https://doi.org/10.1007/BF01339455.

[7] Natanael C. Costa et al. "Ferromagnetism beyond Lieb's theorem". In: *Phys. Rev. B* 94 (15 2016), p. 155107. DOI: 10.1103/PhysRevB.94.155107. URL: https://link.aps.org/doi/10.1103/PhysRevB.94.155107.

[8] "Electron correlations in narrow energy bands". In: *Proceedings of the Royal Society of London A: Mathematical, Physical and Engineering Sciences* 276.1365 (1963), pp. 238–257. ISSN: 0080-4630. DOI: 10.1098/rspa.1963.0204. eprint: http://rspa.royalsocietypublishing.org/content/276/1365/238.full.pdf. URL: http://rspa.royalsocietypublishing.org/content/276/1365/238.

[9] Patrik Fazekas. *Lecture notes on electron correlation and magnetism*. Mod. Condensed Matter Phys. Singapore: World Scientific, 1999. URL: http://cds.cern.ch/record/334821.

[10] "Feynman Diagrams for Condensed Matter Physics". In: *Topics and Methods in Condensed Matter Theory: From Basic Quantum Mechanics to the Frontiers of Research*. Berlin, Heidelberg: Springer Berlin Heidelberg, 2007, pp. 217–256. ISBN: 978-3-540-70727-1. DOI: 10.1007/978-3-540-70727-1_11. URL: https://doi.org/10.1007/978-3-540-70727-1_11.

[11] Mingxuan Fu et al. "Evidence for a gapped spin-liquid ground state in a kagome Heisenberg antiferromagnet". In: *Science* 350.6261 (2015), pp. 655–658.

[12] F. Gebhard. *The Mott Metal-Insulator Transition: Models and Methods*. Springer Series in Solid-State Sciences Nr. 137. Springer, 1997. ISBN: 9783540614814. URL: https://books.google.at/books?id=U8UrAAAAYAAJ.

[13] Antoine Georges et al. "Dynamical mean-field theory of strongly correlated fermion systems and the limit of infinite dimensions". In: *Reviews of Modern Physics* 68.1 (1996), p. 13.

[14] P. Gunacker et al. "Worm-improved estimators in continuous-time quantum Monte Carlo". In: *Phys. Rev. B* 94 (12 2016), p. 125153. DOI: 10.1103/PhysRevB.94.125153. URL: https://link.aps.org/doi/10.1103/PhysRevB.94.125153.

[15] Patrik Gunacker. *Kontinuumsszeit-Quanten-Monte-Carlo in der Hybridisierungs-Expansion: Implementierungen und Anwendungen*. eng. Wien, 2018. URL: https://resolver.obvsg.at/urn:nbn:at:at-ubtuw:1-114444.

[16] Tian-Heng Han et al. "Fractionalized excitations in the spin-liquid state of a kagome-lattice antiferromagnet". In: *Nature* 492.7429 (2012), p. 406.

[17] K. Held. "Dynamical Vertex Approximation". In: *ArXiv e-prints* (Nov. 2014). arXiv: 1411.5191 [cond-mat.str-el].

[18] K. Held. "Electronic Structure Calculations using Dynamical Mean Field Theory". In: *eprint arXiv:cond-mat/0511293* (Nov. 2005). eprint: cond-mat/0511293.

[19] J. E. Hirsch. "Discrete Hubbard-Stratonovich transformation for fermion lattice models". In: *Phys. Rev. B* 28 (7 1983), pp. 4059–4061. DOI: 10.1103/PhysRevB.28.4059. URL: https://link.aps.org/doi/10.1103/PhysRevB.28.4059.

[20] V. I. Iglovikov, E. Khatami, and R. T. Scalettar. "Geometry Dependence of the Sign Problem". In: *Phys. Rev. B 92, 045110 (2015)* (Jan. 12, 2015). DOI: 10.1103/PhysRevB.92.045110. arXiv: 1501.02832v3 [cond-mat.str-el].

[21] V. I. Iglovikov et al. "Superconducting transitions in flat-band systems". In: *Phys. Rev. B* 90 (9 2014), p. 094506. DOI: 10.1103/PhysRevB.90.094506. URL: https://link.aps.org/doi/10.1103/PhysRevB.90.094506.

[22] Mark Jarrell and James E Gubernatis. "Bayesian inference and the analytic continuation of imaginary-time quantum Monte Carlo data". In: *Physics Reports* 269.3 (1996), pp. 133–195.

[23] Radi A. Jishi. *Feynman Diagram Techniques in Condensed Matter Physics*. Cambridge University Press, 2013. DOI: 10.1017/CBO9781139177771.

[24] Gyu-Boong Jo et al. "Ultracold Atoms in a Tunable Optical Kagome Lattice". In: *Phys. Rev. Lett.* 108 (4 2012), p. 045305. DOI: 10.1103/PhysRevLett.108.045305. URL: https://link.aps.org/doi/10.1103/PhysRevLett.108.045305.

[25] Josef Kaufmann. *Python Package ana cont*. 2018. URL: https://github.com/josefkaufmann/ana_cont.

[26] Ehsan Khatami, Rajiv R. P. Singh, and Marcos Rigol. "Thermodynamics and phase transitions for the Heisenberg model on the pinwheel distorted kagome lattice". In: *Phys. Rev. B* 84 (22 2011), p. 224411. DOI: 10.1103/PhysRevB.84.224411. URL: https://link.aps.org/doi/10.1103/PhysRevB.84.224411.

[27] NB Kopnin, TT Heikkilä, and GE Volovik. "High-temperature surface superconductivity in topological flat-band systems". In: *Physical Review B* 83.22 (2011), p. 220503.

[28] Che-Rung Lee, Zhi-Hung Chen, and Quey-Liang Kao. "Parallelizing the hamiltonian computation in dqmc simulations: Checkerboard method for sparse matrix exponentials on multicore and gpu". In: *Parallel and Distributed Processing Symposium Workshops & PhD Forum (IPDPSW), 2012 IEEE 26th International*. IEEE. 2012, pp. 1889–1897.

[29] Ryan Levy, J.P.F. LeBlanc, and Emanuel Gull. "Implementation of the maximum entropy method for analytic continuation". In: *Computer Physics Communications* 215.Supplement C (2017), pp. 149 –155. ISSN: 0010-4655. DOI: https://doi.org/10.1016/j.cpc.2017.01.018. URL: http://www.sciencedirect.com/science/article/pii/S0010465517300309.

[30] Hai-Jun Liao et al. "Gapless spin-liquid ground state in the S= 1/2 kagome antiferromagnet". In: *Physical review letters* 118.13 (2017), p. 137202.

[31] Elliott H. Lieb. "Two theorems on the Hubbard model". In: *Phys. Rev. Lett.* 62 (10 1989), pp. 1201–1204. DOI: 10.1103/PhysRevLett.62.1201. URL: https://link.aps.org/doi/10.1103/PhysRevLett.62.1201.

[32] A. K. McMahan et al. "Volume-Collapse Transitions in the Rare Earth Metals". In: *J. Comput.-Aided Mater. Des. 5, 131 (1998)* (May 6, 1998). DOI: 10.1023/A:1008698422183. arXiv: cond-mat/9805064v1 [cond-mat.str-el].

[33] Walter Metzner and Dieter Vollhardt. "Correlated lattice fermions in d=∞ dimensions". In: *Physical review letters* 62.3 (1989), p. 324.

[34] Andreas Mielke. "Ferromagnetism in the Hubbard model and Hund's rule". In: *Physics Letters A* 174.5-6 (1993), pp. 443–448.

[35] A. Montorsi. *The Hubbard Model: A Reprint Volume*. World Scientific, 1992. ISBN: 9789810205867. URL: https://books.google.at/books?id=QoGl8H7tphYC.

[36] N F Mott. "The Basis of the Electron Theory of Metals, with Special Reference to the Transition Metals". In: *Proceedings of the Physical Society. Section A* 62.7 (1949), p. 416. URL: http://stacks.iop.org/0370-1298/62/i=7/a=303.

[37] M. R. Norman. "Colloquium, Herbertsmithite and the search for the quantum spin liquid". In: *Rev. Mod. Phys.* 88 (4 2016), p. 041002. DOI: 10.1103/RevModPhys.88.041002. URL: https://link.aps.org/doi/10.1103/RevModPhys.88.041002.

[38] Thereza Paiva et al. "Signatures of Spin and Charge Energy Scales in the Local Moment and Specific Heat of the Two-Dimensional Hubbard Model". In: *Phys. Rev. B 63, 125116 (2001).* (Aug. 2, 2000). DOI: 10.1103/PhysRevB.63.125116. arXiv: cond-mat/0008044v1 [cond-mat.str-el].

[39] Warren E Pickett and David J Singh. "LuNi 2 B 2 C: A novel Ni-based strong-coupling superconductor". In: *Physical review letters* 72.23 (1994), p. 3702.

[40] William H. Press et al. *Numerical Recipes 3rd Edition: The Art of Scientific Computing.* 3rd ed. New York, NY, USA: Cambridge University Press, 2007. ISBN: 0521880688, 9780521880688.

[41] M. Rasetti. *The Hubbard Model: Recent Results.* International journal of modern physics / B. World Scientific, 1991. ISBN: 9789810206239. URL: https://books.google.at/books?id=pIpwtAEACAAJ.

[42] G Rohringer et al. "Diagrammatic routes to nonlocal correlations beyond dynamical mean field theory". In: *Reviews of Modern Physics* 90.2 (2018), p. 025003.

[43] Tôru Sakai and Hiroki Nakano. "Gapless quantum spin liquid of the kagome-lattice antiferromagnet". In: *Polyhedron* 126 (2017), pp. 42 –44. ISSN: 0277-5387. DOI: https://doi.org/10.1016/j.poly.2017.01.012. URL: http://www.sciencedirect.com/science/article/pii/S0277538717300256.

[44] Raimundo R. dos Santos. "Introduction to Quantum Monte Carlo simulations for fermionic systems". In: *Braz. J. Phys. 33, 36 (2003)* (Mar. 26, 2003). arXiv: cond-mat/0303551v1 [cond-mat.str-el].

[45] Nicholas E. Sherman, Takashi Imai, and Rajiv R. P. Singh. "Nuclear relaxation rates in the Herbertsmithite Kagome antiferromagnets ZnCu3(OH)6Cl2". In: *Phys. Rev. B 94, 140415(R) (2016)* (Sept. 1, 2016). DOI: 10.1103/PhysRevB.94.140415. arXiv: 1609.00422v1 [cond-mat.str-el].

[46] Nicholas E. Sherman and Rajiv R. P. Singh. "Structure Factors of the Kagome-Lattice Heisenberg antiferromagnets at finite temperatures". In: *Phys. Rev. B 97, 014423 (2018)* (Nov. 15, 2017). DOI: 10.1103/PhysRevB.97.014423. arXiv: 1711.05375v1 [cond-mat.str-el].

[47] Matthew P. Shores et al. "A Structurally Perfect S = 1/2 Kagomé Antiferromagnet". In: *Journal of the American Chemical Society* 127.39 (2005). PMID: 16190686, pp. 13462–13463. DOI: 10.1021/ja053891p. eprint: http://dx.doi.org/10.1021/ja053891p. URL: http://dx.doi.org/10.1021/ja053891p.

[48] Rajiv R. P. Singh and David A. Huse. "Ground state of the spin-1/2 kagome-lattice Heisenberg antiferromagnet". In: *Phys. Rev. B* 76 (18 2007), p. 180407. DOI: 10.1103/PhysRevB.76.180407. URL: https://link.aps.org/doi/10.1103/PhysRevB.76.180407.

[49] J. C. Slater and G. F. Koster. "Simplified LCAO Method for the Periodic Potential Problem". In: *Phys. Rev.* 94 (6 1954), pp. 1498–1524. DOI: 10.1103/PhysRev.94.1498. URL: https://link.aps.org/doi/10.1103/PhysRev.94.1498.

[50] Klaus Steiner. *PyMPDQMC*. 2018. URL: https://github.com/ksteiner92/PyMPDQMC.

[51] Hal Tasaki. "From Nagaoka's Ferromagnetism to Flat-Band Ferromagnetism and BeyondAn Introduction to Ferromagnetism in the Hubbard Model". In: *Progress of Theoretical Physics* 99.4 (1998), pp. 489–548. DOI: 10.1143/PTP.99.489. eprint: /oup/backfile/content_public/journal/ptp/99/4/10.1143/ptp.99.489/2/99-4-489.pdf. URL: http://dx.doi.org/10.1143/PTP.99.489.

[52] J Vannimenus and G Toulouse. "Theory of the frustration effect. II. Ising spins on a square lattice". In: *Journal of Physics C: Solid State Physics* 10.18 (1977), p. L537.

[53] Markus Wallerberger et al. "w2dynamics: Local one- and two-particle quantities from dynamical mean field theory". In: (Jan. 30, 2018). arXiv: 1801.10209v2 [cond-mat.str-el].

[54] Gian-Carlo Wick. “The evaluation of the collision matrix”. In: *Physical review* 80.2 (1950), p. 268.

[55] Simeng Yan, David A. Huse, and Steven R. White. “Spin-Liquid Ground State of the S = 1/2 Kagome Heisenberg Antiferromagnet”. In: *Science* 332.6034 (2011), pp. 1173–1176. ISSN: 0036-8075. DOI: 10.1126/science.1201080. eprint: http://science.sciencemag.org/content/332/6034/1173.full.pdf. URL: http://science.sciencemag.org/content/332/6034/1173.

[56] Yuanyuan Zong et al. “Observation of localized flat-band states in Kagome photonic lattices”. In: *Opt. Express* 24.8 (2016), pp. 8877–8885. DOI: 10.1364/OE.24.008877. URL: http://www.opticsexpress.org/abstract.cfm?URI=oe-24-8-8877.